



Krypton storage capacity of the Earth's lower mantle

A.D. Rosa, Mohamed Ali M.A. Bouhifd, G. Morard, R. Briggs, G. Garbarino, T. Irifune, O. Mathon, S. Pascarelli

► To cite this version:

A.D. Rosa, Mohamed Ali M.A. Bouhifd, G. Morard, R. Briggs, G. Garbarino, et al.. Krypton storage capacity of the Earth's lower mantle. *Earth and Planetary Science Letters*, 2020, 532, pp.116032. 10.1016/j.epsl.2019.116032 . hal-02453936

HAL Id: hal-02453936

<https://uca.hal.science/hal-02453936>

Submitted on 16 Nov 2020

HAL is a multi-disciplinary open access archive for the deposit and dissemination of scientific research documents, whether they are published or not. The documents may come from teaching and research institutions in France or abroad, or from public or private research centers.

L'archive ouverte pluridisciplinaire **HAL**, est destinée au dépôt et à la diffusion de documents scientifiques de niveau recherche, publiés ou non, émanant des établissements d'enseignement et de recherche français ou étrangers, des laboratoires publics ou privés.

Krypton storage capacity of the Earth's lower mantle

A.D. Rosa¹, M.A. Bouhifd², G. Morard³, R. Briggs⁴, G. Garbarino¹, T. Irifune⁵,

O. Mathon¹, S. Pascarelli¹

¹ *European Synchrotron Radiation Facility (ESRF), 71, Avenue des Martyrs, Grenoble, France.*

² *Laboratoire Magmas et Volcans, Université Clermont Auvergne, CNRS, IRD, OPGC, F-63000 Clermont-Ferrand, France.*

³ *Sorbonne Université, Muséum National d'Histoire Naturelle, UMR CNRS 7590, IRD, Institut de Minéralogie, de Physique des Matériaux et de Cosmochimie, IMPMC, 75005 Paris, France.*

⁴ *Lawrence Livermore National Laboratory, Livermore, CA, United States of America*

⁵ *Geodynamics Research Center, Ehime University, 2-5 Bunkyo-cho, Matsuyama 790-8577, Japan.*

Abstract

Noble gases are important geochemical tracers allowing reconstructing global volatile cycles in Earth's reservoirs. To constrain these fundamental processes, precise data on their partitioning behavior at deep Earth conditions are needed. Such data are only available at moderate pressures up to 25 GPa due to experimental challenges. We have investigated the possibility of noble gas storage in the Earth's lower mantle up to 115 GPa. We studied the incorporation of krypton in the second most abundant lower mantle mineral ($\text{Mg}_{1-x}\text{Fe}_x\text{O}$) (ferropericlase) as well as in liquid metal-alloys by performing experiments up to 115 GPa and 3700 K using the laser-heated diamond anvil cell coupled to post-mortem EMPA analysis and X-ray absorption spectroscopy. The results reveal that, at these extreme conditions, up to 3 wt.% of krypton can be stored in ($\text{Mg}_{1-x}\text{Fe}_x\text{O}$) and 3000 ppm in the Fe-rich liquid metal. For both phases the storage capacities increase with pressure (between 40 GPa and 60 GPa) at a constant high temperature of 2300 K. Fpc has never been considered as a NG host, despite being the second most abundant mineral in the Earth's LM. Using recent accurate

compressibility data, we demonstrate that a substitution of krypton into the anion site of $(\text{Mg}_{1-x}\text{Fe}_x)\text{O}$ in form of neutral oxygen Schottky defects at diluted lower mantle conditions is possible. This noble gas incorporation mechanism is in agreement with a previous study on bridgmanite. We show that $(\text{Mg}_{1-x}\text{Fe}_x)\text{O}$ exhibits higher noble gas storage capacities than bridgmanite through the lower mantle using lattice strain modelling and including experimental solubility and thermoelastic data for neon, argon, krypton and xenon. We also demonstrate that both phases exhibit the highest solubilities for argon and krypton. We used the solubility data from lattice strain modelling to predict noble gas abundances stored in the solid lower mantle after magma ocean crystallization. The modelled abundances show apparent similarities with estimates for the deep noble gas reservoir that are based on either ^3He abundances in ocean island basalts or radiogenic ^{40}Ar abundances in the bulk Earth. This strongly indicates that the crystalline lower mantle may play an important role as deep noble gas storage reservoir. We propose, based on considerations on noble gas replenishment from the lower mantle to the atmosphere, that the lower mantle can only contribute to a small fraction of the present-day atmospheric noble gases. This suggests that the lower mantle is an un-degassed reservoir.

Highlights

1. Krypton storage capacities of $(\text{Mg,Fe})\text{O}$ and metal alloys up to 115 GPa and 3700 K
2. Storage capacities of lower mantle minerals are greater than those of metallic melts
3. Zero-charged krypton is incorporated in neutral oxygen defects of $(\text{Mg,Fe})\text{O}$
4. The lower mantle could be a reservoir for noble gases through geologic times

1. Introduction

Noble gases (NGs) are important geochemical tracers allowing reconstructing atmospheric evolution processes over geological time scales (*i.e.*, [Moreira, 2013](#)). NG isotope patterns of oceanic island and mid oceanic ridge basalts (OIB and MORB) provide evidence for two different mantle NG reservoirs: the strongly degassed source of MORBs and a less degassed primordial reservoir sampled eventually by deeply originating mantle plumes of OIBs ([Allègre and Turcotte, 1986](#); [Marty, 2012](#); [Mukhopadhyay, 2012](#); [Moreira, 2013](#)). The isotopic fingerprints for light NGs including He and Ne, indicate that the deep reservoir must have been created very early during Earth accretion (100 Myrs of solar system history) as it retained a fraction of the implanted proto-solar nebula. Moreover, because the deep reservoir inherits a higher fraction of fissogenic non-degassed xenon (Xe) isotopes than MORBs (formed by radioactive decay of U and Pu), it is assumed that the two reservoirs were decoupled early after Earth accretion (about 4.45 Gyrs ago) (e.g., [Allègre et al., 1983](#); [Pepin and Porcelli, 2006](#); [Mukhopadhyay, 2012](#)).

The size and location of the deep reservoir still remain subjects of debates because of the difficulties to constrain the exact sources and origins of OIBs. Possible candidates have been proposed including the entire lower mantle (LM), the D'' layer and the Earth's core ([Allègre and Turcotte, 1986](#); [Marty, 2012](#); [Mukhopadhyay, 2012](#); [Bouhifd et al., 2013](#); [Moreira and Kunz, 2013](#)).

The solubility data of NGs in different deep mantle and core phases (minerals and melts) could provide important information by identifying in which reservoir NGs have preferentially partitioned during the crystallization of the magma ocean (MO). Previous experimental studies on NG solubilities have revealed their preferential partitioning in silicate melts as compared to minerals at upper mantle (UM) conditions ([Carroll and Stolper, 1993](#);

Matsuda et al., 1993; Brooker et al., 2003; Bouhifd and Jephcoat, 2006; Heber et al., 2007; Watson et al., 2007). Because NGs exhibit also higher diffusivities in melts than in silicates at shallow mantle conditions (Hofman and Hart, 1978), they are efficiently extracted from the mantle through partial melting and back-recycled into the atmosphere *via* volcanism.

In contrast to the observed NGs incompatibilities in silicates at shallow mantle conditions, Shcheka and Keppler (2012) reported high compatibilities of argon (Ar) and krypton (Kr) in the LM mineral bridgmanite (Bg). They reported solubilities of up to 1 wt.% for Ar, 3000 ppm for Kr and 300 ppm for Xe at 25 GPa and 2100 K and proposed that NGs are most likely incorporated in neutral oxygen vacancies. Interestingly, Ar solubilities measured in chondritic melts at similar conditions are below those of Bg (Bouhifd and Jephcoat, 2006), while those measured in pure SiO₂ melts are in the same order of magnitude (~ 1 wt.% Ar) (Niwa et al., 2013). These discrepancies on NG solubilities in silicate melts might be related to compositional effects. Overall, previous observations suggest that LM minerals may exhibit higher NG solubilities and bear the capacity to store NGs over geological time scales. Shcheka and Keppler (2012) also proposed that the reinjection of these deeply stored NGs, predominantly composed of Ar and Kr, through mantle melting may explain the Xe depletion signature of the Earth atmosphere (Pepin and Porcelli, 2002). However, the contribution of LM NGs to the present-day atmospheric signature may be only minor as the source of atmospheric xenon has been recently identified to be cometary (about $22 \pm 5\%$), in addition to chondritic (or solar) xenon (Avice et al., 2017; Marty et al., 2017).

In the present study, we provide information on NG storage in LM minerals and melts by investigating experimentally the maximum solubility of Kr in ferropericlase (Mg,Fe)O and different metal alloys up to the conditions of the bottom of the LM (115 GPa and 3700 K). Our data reveal that ferropericlase can retain up to 3 wt.% of Kr. This is 5 to 10 times more than Bg in the Earth's LM and metallic melts of the outer Earth's core, respectively. Therefore, we

propose that ferropericlasite may play an important role in NG retention during magma ocean crystallization and that the LM could potentially be a deep NG reservoir.

2. Methods

Our experiments are aimed at constraining the Kr storage capacities of Fpc (Mg,Fe)O and different metal alloy melts up to the pressure and temperature (P/T) conditions of the bottom of the LM (115 GPa and 3700 K). We have performed laser-heated diamond anvil cell (LH-DAC) experiments at the X-ray absorption (XAS) beamline ID24 of the ESRF. Post-mortem EMPA measurements and XAS analysis were used to precisely quantify and characterize the incorporation of NGs in the quenched samples.

2.1 Starting materials

We used synthetic metal-alloy foils of $\text{Fe}_{88}\text{S}_{12}$ and $\text{Fe}_{85}\text{Ni}_{15}\text{S}_{10}$ which were produced by an ultra-rapid quench method at the ICMPE (Institut de Chimie et des Matériaux de Paris-Est, Paris, France) (Morard et al., 2011). This technique guarantees a void free homogenous composition and a small sample thickness (5-7 μm). Nickel foils from Goodfellow (trace element basis 99.95%), MgO powder from Sigma Aldrich (catalogue number: 34279) and Kr gas having a purity of 99.99% from Air Products were used as high-purity starting materials. The MgO powder was heated above 393 K to remove the moisture contamination from the air. After heating, it was compressed under nitrogen atmosphere to produce thin pellets of 5-10 μm thickness using a diamond anvil cell without gasket. In such a device, the MgO powder is subjected to a high-pressure sintering process (up to 10 GPa) which leads to a highly compacted material with a very low porosity. The resulting metal foils and MgO pellets were stored in a dry atmosphere before sample loading.

2.2 High pressure and temperature experiments

Membrane driven diamond anvil cells (DAC) of the LeToullec design were used to generate high pressures. The DACs were equipped with single-crystal or nano-polycrystalline diamonds. The dimensions of diamond anvil culets varied between 150 and 400 μm depending on the target pressure (40-115 GPa). For all experiments, we have employed pre-indented Re gaskets. A hole drilled at the center of the gasket was used as sample chamber (**Table 1**).

In total seven samples were prepared and investigated (**Table 1**). Two samples were prepared using a 5 μm thick metal foil of $\text{Fe}_{88}\text{S}_{12}$ sandwiched between two MgO pellets (Cell_1-2, **Table 1**). The upper MgO pellet was placed such that it only partly covered the metal foil (**Figure 1**). These samples were used to investigate the different krypton storage capacities of MgO and $\text{Fe}_{88}\text{S}_{12}$ at identical T but different P conditions. We employed compacted MgO pellets because single-crystals of MgO have a high risk of breaking upon compression, especially in the present sample geometry.

Five other sample assemblies were prepared using $\text{Fe}_{88}\text{S}_{12}$, $\text{Fe}_{85}\text{Ni}_{15}\text{S}_{10}$ or Ni placed on a KCl disc of 5-10 μm thickness (Cell_3-7, **Table 1**). These samples were used to study the Kr incorporation in metallic melts as a function of the composition and P/T conditions.

In all experiments a ruby sphere was loaded on the rim of the Re gasket hole for pressure monitoring. The remaining sample chamber cavity was then filled with supercritical Kr using the gas-loading device at the ESRF which was purged twice with Kr gas to avoid contamination from the air. The samples were stored and handled in dry nitrogen atmosphere or under vacuum during loading and after the laser heating runs.

At the target pressure, the samples were single-sided laser-heated using the laser-heating system installed at ID24 (**Supplementary Information**). The metal foils sandwiched between two MgO pellets were heated at the contact surface of Kr and the metal (and MgO)

(**Figure 1**). The metal foils placed only on a KCl disk were heated on the metal(-alloy) contact surface to Kr in several positions. The laser hot-spot diameter varied between 20 and 60 μm depending on the sample size and pressure. The temperature was raised up to 1800-3700(150) K by adjusting the laser power and maintained for 20-30 minutes to reach equilibrium conditions.

At the P/T conditions of the experiments, Kr and MgO remained solid (Jephcoat, 1998; Du and Lee, 2014). This excludes the formation of supercritical Kr or Kr gas during the experimental runs. In contrast, the experimental temperatures exceeded by several hundred degrees the liquidus temperature of metal foils (except for the heating spot 2 in Cell_7) (Morard et al., 2008, 2011; Lord et al., 2014; Mori et al., 2017).

2.3. Elemental concentration measurements

Scanning electron microscope (SEM) maps of recovered samples were acquired with a small beam size of 2 μm and at an acceleration voltage of 20 kV, except for Cell_7, to determine the distribution of Fe, Si, O, S, Mg and Ni, using the SEM microscope installed at the “Laboratoire Magmas et Volcans” in Clermont-Ferrand (France) (**Figure S1**). Precise quantitative concentrations of Kr, Fe, Ni, S, and Mg in the quenched samples were then determined from electron micro-probe analyzer (EMPA) measurements using a Cameca SX100 micro probe (Clermont-Ferrand, France) (**Figure 2a**). The signal intensity for Kr was calibrated following the procedure described in Shcheka and Keppler (2012) for three detector crystals using 7 different elemental standards adjacent to Kr (**Figure S2**). This calibration method resulted in a Kr detection limit of 100 ppm. For Fe, Ni, S, and Mg an EMPA electron beam current of 15 nA was employed while for Kr a current of 40 nA was used. The EMPA electron beam size was 1-2 μm , and after each analysis, the beam position was controlled to ensure the beam spot position stability. Those measurements for which the electron beam has

167 moved were discarded. Measurements with analytical totals within 95% were included in the
168 analysis in addition to few data with totals above 85%. Measurements with totals below 85%
169 were excluded.

170 In two cases, the EMPA measurements of the laser-heated iron-alloy areas resulted in
171 surface structure changes due to the impinging electron beam. This effect is most likely related
172 to sample disproportions linked to the metastable nature of the quenched glasses. We therefore
173 discarded these measurements. All Kr concentrations obtained from EMPA measurements in
174 the samples and different phases are listed in **Table S1**, except for Cell_5 for which the
175 measured concentrations fell below the detection limit and Cell_7 for which EMPA
176 measurements have not been performed.

177 **2.4. XRF and XAS experiments**

178 X-ray absorption spectroscopy (XAS) is a powerful technique to probe the local
179 structural environment of diluted elements embedded in crystalline or glass matrixes. XAS data
180 acquired in transmission geometry present the sum of all contributions along the beam
181 pathway. In the present study, the sample configuration was optimized to separate the signal
182 from pure krypton loaded in the sample chamber cavity next to MgO and the one from the
183 krypton incorporated in the crystal after laser-heating (**Figure 1**). At ID24 *in-situ* XAS
184 transmission measurements on Kr retained in the oxide during heating were unfortunately not
185 possible due to the low concentrations of Kr retained in the laser-heated hotspot and the large
186 X-ray beam size at the Kr K-edge (50 μm at full width half maximum) which exceeded the
187 laser hotspot size (**Figure 1**).

188 A much smaller beamsizes (submicron) than presently available is required to conduct
189 such experiments *in-situ* during heating or after heating and at high pressure. Therefore, only
190 XAS data of pure Kr upon compression and after heating could be collected at ID24. The

structural environments around Kr retained in the heating spot were therefore investigated only on quenched samples by XAS. These measurements were conducted in backscattered fluorescence geometry at the ESRF beamline BM23 using a highly focused beam of $5 \times 5 \mu\text{m}^2$ (**Supplementary Information**). The measurements were completed by full-multiple scattering calculations to derive the atomic environments around Kr in the quenched samples (**Supplementary Information**).

3. Results and discussion

3.1 Kr concentrations retained in Fpc and metallic melts

Detailed elemental concentrations obtained from EMPA measurements for each sample are listed in **Table S1**. For Cell_1-2, we observed that laser-heating of pure MgO in contact with the $\text{Fe}_{88}\text{S}_{12}$ alloy resulted in the diffusion of Fe into MgO forming Ferropericlasite ($\text{Mg}_{1-x}\text{Fe}_x\text{O}$) with x reaching up to 0.27. In the following, the resulting ($\text{Mg}_{1-x}\text{Fe}_x\text{O}$) phase will be referred to as Fpc.

The EMPA measurements and the XRF and SEM maps revealed that Kr concentrations in Fpc and the metal foils show variations with the distance from the laser hotspot (**Figure 2** and S1, Cell_1, 2 and 6). Interestingly, the Kr contents measured for Fpc samples show a slight decrease with increasing distance from the hotspot (within a diameter of $20 \mu\text{m}$). The observed concentration variations may be related to a partitioning or diffusion process that is sensitive to the temperature decrease with increasing distance from the laser hotspot.

Lateral temperature gradients in the LH-DAC depend on the laser beam shape, as well as the thermal conductivity of the sample and insulating material. We have maximized the laser-heating spot in all experiments in order to reduce the thermal gradients in its center and maximize the area where the concentration measurements were carried out. The measurement

of the thermal gradients across the laser hotspot requires special LH-DAC setups (Campbell, 2008). The present measurements have been performed on a standard system that does not allow such measurements. We therefore assumed temperature gradients between 500-1200 K from the hotspot center to the hot-spot rim for measured hotspot temperatures ranging from 2300 – 3700 K following the observations of Campbell (2008) and Fischer et al. (2015). Due to the micrometric size of the samples, submicron beams would be necessary to better explore the effect of temperature gradients on Kr concentration variations. Such micro-beams are presently not available for standard EMPA instruments.

First order constraints on the relations between temperature, pressure as well as chemical composition and measured Kr contents in the different phases can be obtained by averaging those Kr concentrations measured in the hotspot center (within a diameter of 20 μm) and laser-heating spot rim (within a diameter of 20-40 μm). This procedure allows separating regions in the laser hotspot that exhibit the most homogeneous temperature distributions from those that are subjected to higher T gradients. The P/T conditions of each cell and laser-heated spot together with the resulting averaged Kr concentrations of phases at different distances from the laser hotspot are listed in **Table 1** together with the maximal Kr concentrations measured in each sample and averaged Kr concentrations using all measurements.

The Kr concentrations measured in Fpc in the hotspot center as a function of the pressure, the iron and sulfur content are shown in **Figure 3**. The most striking observations are the high Kr concentrations of almost 3 wt.% in Fpc (**Table 1**, Cell_2) and their increase with pressure (**Figure 3**). We also found that Kr concentrations in Fpc are strongly correlated with the Fe content (**Figure 3a**, taking only the data from the hotspot center). With increasing pressure from 40 to 60 GPa the average Kr and Fe contents in Fpc increase from 1.2(2) to 2.2(5) wt.% and 7(3) to 23(4) wt.%, respectively (**Figure 3a**). For sulfur, we observed the

opposite trend: the averaged sulfur concentrations in Fpc are slightly higher at 40 GPa than at 60 GPa, decreasing from 2.1(4) down to 0.15(5) wt.% (**Figure 3b**).

We observed the highest Fe and Kr concentrations in the center of the laser heated hotspot in Fpc. This excludes a diffusion activated by the thermal gradients (Soret effect) which should normally result in a migration of heavy elements such as Fe or Kr towards the hotspot rim ([Auzende et al., 2008](#)). We considered instead that equilibrium conditions have been achieved during the long laser heating runs at least for Fe in the hotspot center ([Auzende et al., 2008](#)). To understand if the equilibrium conditions for Kr in the entire heating spot (max. 60 microns at 40 GPa) were also reached, the diffusion coefficients for Kr (D_{Kr}) in Fpc at the present experimental conditions are required. These coefficients are however not available. We therefore related the concentration variations of Fe and Kr in the hotspot center in Fpc to the temperature dependent partitioning behavior of Fe and Kr into Fpc.

Kr concentrations in quenched metallic melts as a function of the P/T conditions, distance to the laser-heated hotspot and composition are plotted in **Figure 4**. Molten Ni shows the highest Kr storage capacity, among all investigated metallic melts. It could retain a maximum of 0.77(1) wt.% of Kr at 62(1) GPa and 2800 K (**Table 1**). This value is much larger than for $\text{Fe}_{88}\text{S}_{12}$ and $\text{Fe}_{85}\text{Ni}_{15}\text{S}_{10}$ which respectively exhibit a maximum of 0.38(1) and 0.14(1) wt.% at similar conditions (**Table 1**). Interestingly, the averaged Kr storage capacities of the metallic melts are much lower than those of Fpc (**Figure 3**). Moreover, we did not observe a correlation between the Kr and S contents in $\text{Fe}_{88}\text{S}_{12}$ as in Fpc (**Table S1**).

3.2 Kr partitioning in the lower Earth's mantle

In-situ experiments at the relevant high dilution levels and extreme conditions remain challenging. The present experiments have been performed at Kr-saturated conditions similar to previous large-volume press studies on Bg (Shcheka and Keppler, 2012) or LH-DAC studies on silicate melts (Chamorro-Perez et al., 1996; Bouhifd and Jephcoat, 2006; Bouhifd et al., 2013; Niwa et al., 2013). The derived concentrations in quenched samples of such studies present the upper limit of Kr solubilities in the different phases (Table 1).

We averaged the Kr concentrations from all EMPA measurements within the laser-heated spot in each phase at a certain P/T point to estimate the maximum Kr solubilities as a function of pressure in the different phases (Table 1, column named: everything). We considered that this procedure provides a better statistical measure of Kr retained in the laser hotspot. The resulting maximal Kr solubilities in Fpc are 1.2 and 1.8 wt.% and 0.03 wt.% and 0.15 wt.% for $\text{Fe}_{88}\text{S}_{12}$ at 40 and 60 GPa and 2300 K, respectively. These estimated Kr solubilities are presented in Figure 5a and were used to assess the pressure dependent partitioning coefficients $D_{\text{metal/oxide}}$ shown in Figure 5b (black triangles). The resulting $D_{\text{metal/oxide}}$ values are below unity indicating that Kr preferentially partitions into Fpc. An extrapolation of $D_{\text{metal/oxide}}$ to the core mantle boundary reveals, that the preference for Kr to enter into Fpc prevails, while small amounts of Kr may still be present in the Earth's core.

The present results indicate that Kr is highly soluble in Fpc and to a lesser extent in metallic melts. The liquid Earth's core as well as liquid iron droplets descending within the magma ocean during Earth's core formation would therefore be rather poor in Kr (Figure 5). Our data suggest that for both Fpc and metallic melts the solubility increases with depth. These observations strongly differ from the previously reported Ar solubility decrease in silicate melts beyond 15 GPa (*i.e.*, Bouhifd and Jephcoat, 2006; Niwa et al., 2013). According to Bouhifd

and Jephcoat (2006), the Ar solubility in chondritic melts reduces at 25 GPa to 0.05 wt.%. This is a factor of 10 less than what we estimated for Kr in Fpc at such conditions (0.56 wt.% at 25 GPa). The extrapolation of the data from Niwa et al. (2013) in pure silicate beyond 20 GPa suggests an Ar solubility of 1 wt.% at 25 GPa and a decrease to 0.5 wt.% at 30 GPa. These observations may indicate that Kr is retained in crystalline phases especially at the bottom of the Earth's LM during mantle crystallization. This is due to the probable incompatibility of NGs in ultra-dense silicate melts. The solubilities in melts remain however still debated due to the few studies conducted so far. Therefore, a more elaborated discussion on crystal-melt partitioning behavior at LM conditions is not warranted.

Shcheka and Keppler (2012) reported Kr solubilities in Fe-free and Al-bearing bridgmanite from 0.11 to 0.33 wt.% at 25 GPa and 1800 K that increase with the Al content. Using their data, we obtained a partitioning coefficient between bridgmanite (Brg) and Fpc $D_{\text{Fpc/Brg}}$ of 1.69 to 4.9 (9) at ~25 GPa. We found that Fpc can retain a maximum of 3.5 wt.% of Kr (**Figure 5a**) by extrapolating the maximal solubility of Kr in Fpc to the CMB. The lower storage capacity of Bg might be due to the absence of iron in the experiments of Shcheka and Keppler (2012). Iron could indeed play an important role for forming oxygen vacancies. Future studies on NG incorporation in iron-bearing bridgmanite are required to better understand partitioning of NGs between the two main crystalline constituents of the Earth's LM. Overall, Fpc exhibits a higher Kr solubility than Bg and despite Fpc is volumetrically inferior (Fpc:Bg = 20:80 vol.%), it can store up to 45% of the Kr present in the LM.

3.3 Kr incorporation mechanism

The understanding of the microscopic NGs incorporation mechanism in LM solid and liquid phases is fundamental for predicting their partitioning behaviors (Karato, 2016). However, this mechanism remains largely unexplored except for Bg (Shcheka and Keppler, 2012). At moderate P/T conditions, NGs can substitute in open ring structures of hydrous phases (Jackson et al., 2013), or cation positions in silicates (Heber et al., 2007). Because pure Kr exhibits a high compressibility (Rosa et al., 2018), it may also be easily stored in defect vacancies or interstitial sites of phases present at Earth's LM and core conditions.

We calculated the size mismatch between atomic radii of zero charged Kr^0 , Mg^{2+} , O^{2-} and metallic Fe at 2300 K and between 40 and 150 GPa (Figure 6, Supplementary Information) to understand if Kr atoms at Earth's LM conditions can fill vacancies or substitute for atoms in Fpc and/or metallic melts. Interestingly, the size mismatch between Kr^0 and the O^{2-} anion in Fpc is the lowest and remains below 10% (Figure 6b). This indicates that at diluted concentrations of the LM, Kr^0 can be incorporated into a neutral oxygen vacancy such as a Schottky defect. The size mismatch between Kr^0 and O^{2-} decreases with increasing pressure (Figure 6b). The proposed substitution of Kr in neutral oxygen Schottky defects can therefore explain the observed increase in solubility (Figure 3). It can also explain the increasing compatibility of Kr in Fpc with increasing iron content. In Fpc such neutral oxygen vacancies could be preferentially associated to iron defect clusters forming, upon increasing pressure, iron and Fe^{3+} content (Kantor et al., 2009).

If Kr solubility in Fpc is associated to the abundance of Fe^{3+} related vacancies, then solubilities should be sensitive to the oxygen fugacity ($f\text{O}_2$). In the present experiments, the $f\text{O}_2$ can be estimated relatively to the iron-wüstite buffer (IW buffer) using the molar fractions

of Fe in the metal phase and FeO in the mineral phase obtained from EMPA measurements (Table S1). We considered an ideal system and calculated fO_2 using the equation:

$$\log fO_2(\Delta IW) = 2 \log (XFeO_{\text{silicate}} / XFe_{\text{metal}})$$

where $XFeO_{\text{mineral}}$ and XFe_{metal} are the molar fractions of FeO and Fe in the mineral and metallic phases, respectively. We have obtained $\log fO_2$ values ranging from -2.1(3) to -1.5(2) at pressures between 40 to 60 GPa and 2300 K. These values are consistent with those obtained in previous works conducted at comparable conditions (Fischer et al., 2015) and can explain the observed correlation of Kr solubility increase with Fe^{3+} abundance. The redox conditions for the accreting mantle have been estimated to range between 4 and 2 log units below the IW buffer (Rubie et al., 2011). This confirms that the present experiments have been conducted at similar or slightly more oxidizing conditions than those of the early Earth.

Recently, an incorporation of single Kr atoms in neutral Schottky defects associated with oxygen vacancies has been also evidenced from XAS measurements of Kr-implanted UO_2 for low Kr concentrations of 0.5 at.% and at ambient conditions (Martin et al., 2015). Oxygen vacancy substitution has been also proposed for the incorporation of Ar, Kr and Xe in Bg based on lattice strain modelling (Shcheka and Keppler, 2012; Karato, 2016).

For molten $Fe_{88}S_{12}$ our calculations have revealed a large radii mismatch between Fe^0 and Kr^0 in the pressure range of 60-150 GPa, with Kr being 30% smaller than Fe^0 (Figure 6b). We propose that Kr is entrapped in interstitial voids of the metallic liquid structure because of the likely Kr diffusion in the low viscous metallic melt. Such an interstitial diffusion mechanism is consistent with the general concept of NG incorporation in silicate melts (Carroll and Stolper, 1993; Brooker et al., 2003; Heber et al., 2007). Detailed atomistic crystal and melt lattice calculations, that are beyond the scope of the present study, are required to better

constrain the potential incorporation sites of NGs in these systems at lower Earth's mantle conditions.

3.4 Local atomic environment of Kr in quenched samples

The present study is the first attempt to characterize the incorporation mechanism of NGs in quenched LM minerals directly using XAS (**Supplementary Information**). The extended X-ray absorption fine structure (EXAFS) which corresponds to the X-ray energy domain located 1000 eV above the absorption edge, is highly sensitive to the distribution and sort of nearest-neighboring atoms. EXAFS data collected at the Kr K-edge demonstrate the existence of a highly disordered first coordination shell that is characterized by a large distribution of inter-atomic distances and different coordinating atomic species including Kr, Fe or Mg (**Figure S3**). The X-ray absorption near edge structure (XANES) which corresponds to the energy region that extends ~100 eV from the absorption edge, provides information on the local site symmetry of the absorbing atom and sort of neighbouring atoms on the medium range scale (second and third coordination shells). A clear similarity between the spectra of Kr retained in quenched samples and those of liquid and solid krypton is apparent (**Figure S4**). This suggests that Kr could partly have, as nearest neighbor, another Kr atom with a similar symmetrical arrangement as pure liquid or solid fcc Kr under pressure. A comparison of the experimental and calculated XANES spectra shows that Kr is most likely incorporated in 6-fold coordinated vacancies surrounded by Fe, and Mg as next nearest neighbors (**Figure S4-5**). The potential substitution of Mg or Fe by Kr is a very unlikely scenario because, in this case, the calculated XANES spectra exhibit a significantly different shape of the white line (**Figure S5**). The local environment of Kr in quenched Fpc is disordered and composed of Mg, Fe and Kr with various amounts as nearest neighbors. The shift of the white line energy in the sample spectra relatively to those of Kr gas clearly demonstrates that Kr is retained under

compressive strains in the quenched samples (of up to 8 GPa, see **Supplementary Information**).

An explanation for the observed highly distorted Kr environments could be the significant expansion of the previously homogeneously distributed Kr atoms during *P/T* quenching. Quenching from 40 GPa leads to a volume expansion of more than 50% for Kr (Rosa et al., 2018) resulting in the generation of large lattice strains in the host sites. These lattice strains can induce short range diffusion of Kr and lattice re-arrangement leading to the formation of defect clusters of sub-nanometric size. This type of cluster formation has been already reported for implanted samples such as MgO (Norton et al., 1992; Noordhuis and De Hosson, 1991). We do not consider that hydrous fluid inclusions containing Kr have formed in our samples. As outlined above in the methods section, we have employed pre-heated MgO powder as well as metal foils stored under vacuum in a desiccator to avoid moisture contamination. In addition, the sample was assembled and sealed in nitrogen atmosphere before loading with Kr in a gas-loading device.

We consider that it is very unlikely that Kr was substantially trapped on grain boundaries between (Mg,Fe)O crystals during the experiments, as we have employed pre-compressed (dried, water-free) MgO pellets. These pellets were made from a MgO powder that was highly compacted in a DAC. In such device, the MgO powder is subjected to a high pressure sintering process (up to 10 GPa) which leads to a highly densified material with low to negligible porosity. Also, similar XAS data of Kr were obtained with samples prepared using a very different synthesis method. Indeed, the iron-alloy foils have been obtained using sputtering methods, a technique that leads to compact foils without voids. Moreover, grain boundary contamination or formation of Kr blebs would lead to constant Kr concentrations in the samples independently of the experimental conditions while we observe an increase of the

Kr concentrations with pressure that is consistent with the predictions of [Shcheka and Keppler \(2012\)](#).

TEM measurements could provide information about the Kr environment in the quenched samples. Such studies on Kr contained in MgO have been previously performed on thin ion-implanted MgO discs that did not require polishing ([Norton et al., 1992](#)). The samples produced in the present study would however require polishing due to the underlying iron foil. We did not perform such measurements because this type of polishing procedure would lead to NG release. In addition, TEM measurements can be only performed on quenched samples that are altered by the significant expansion of Kr once released to room pressure ([Tan et al., 1991](#); [Norton et al., 1992](#); [Martin et al., 2015](#)).

In summary, based on the atomic radii mismatch calculations, we find that Kr incorporated in Fcp *via* a vacancy substitution mechanism at high P/T conditions is possible. Moreover, as Kr remains solid at the high P/T conditions of the experiments and the starting materials employed are void free due to the pre-compressing treatment or used synthesis methods, it is unlikely that Kr blebs form inside Fpc and the metallic foils. The formation of Kr blebs at the surface of Fpc and the metallic foils can be excluded because the experimental XANES spectra clearly demonstrate that Kr is retained under a high compressive stress of up to 8 GPa (**Figure S4, S6**) that can only be sustained in the bulk and not on the surface of the samples. Therefore, we propose that the observed Kr concentrations are due to diffusion processes that took place at high P/T conditions. The precipitation of NG nano-impurity clusters related to Kr exsolution are induced during quenching. We note that sub-nanometric Kr clusters potentially formed in the quenched samples have a minor influence on the conducted EMPA measurements. The electron beam size for EMPA measurements was in the range of 2 μm . Therefore, the sampling was conducted on several sub-(nanometric) impurity clusters as well as on cluster free-areas during one measurement.

4. Implications

4.1. NGs solubilities in the lower mantle minerals

The present experimental results reveal that Fpc can retain 5 times more Kr than Fe-free and Al-bearing Bg in the Earth's uppermost LM and 10 times more than the liquid Earth's outer core. Our results suggest that a larger proportion of the mantle's Kr is stored by Fpc than previously thought. In order to constrain the solubilities of Ne, Ar, Kr and Xe through the LM (25-120 GPa and 1900-2500 K), we performed lattice strain modelling (LSM) (Blundy and Wood, 2003) assuming that NGs enter in neutral oxygen vacancies of Fpc and Bg.

This LSM allowed us predicting solubilities through the mantle for the suite of NGs. NGs exhibit high compressibilities and it is therefore important to include their volumetric variations through the LM. The coordination number is another parameter that has a significant influence on the host site and noble gas radii (Zhang and Zhu, 1995). In the present LSM approach, the radii of NGs and those of the host sites were fixed to calculated values obtained using thermoelastic and crystal-chemistry data (coordination dependent atomic radii size). Similarly, the host site flexibility was fixed to the calculated values extracted from thermoelastic data (Supplementary Information).

In our LSM, we only used the maximal solubility of the site as fitted parameter. This differs from the classical approach for which three parameters (the maximal solubility of the site, the site flexibility and the host site radius) are normally adjusted. We found that the solubility data of Shcheka and Keppler (2012) can be well reproduced with the present LSM (Figure 7). This suggests that the present approach is appropriate and can be used for predicting NG solubilities in a host lattice site at the extreme P/T conditions of the lower mantle and beyond.

The obtained NGs solubilities of the two major LM minerals exhibit different evolutions through the LM (**Figure 7**). For Fpc, the solubilities increase with depth for all NGs while, for Bg, the NGs solubilities decrease with depth except for Xe. This contrasting behavior can be explained by the difference in the mechanical properties of Fpc and Bg. Fpc is indeed softer than Bg and the radius of the oxygen site in Fpc exhibits a higher reduction with increasing depth. Moreover, in the investigated P/T conditions, the NGs exhibit a similarly high compressibility as Fpc.

4.2. NG retention in the lower mantle during magma ocean crystallization

Our lattice strain modelling results reveal that the LM phase assemblage Fpc and Bg retains efficiently Ar and Kr and to a lesser extend Ne and Xe. The present solubility data are representative for NG saturated conditions and can therefore be only applied to crystallization conditions in presence of a volatile saturated liquid or melt phase. Presently, two models describing the crystallization of the magma ocean (MO) in the deep primitive Earth have been reported: (1) the classical solidification model from the bottom to the top ([Solomatov and Stevenson, 1993](#)) and (2) the more recent model that propose the onset of solidification in the mid-mantle ([Labrosse et al., 2007](#)). For both models crystallization of LM minerals at NG saturated conditions may have occurred (**Supplementary Information**). Our model is independent of the type of lower mantle crystallization (either bottom-up or mid-mantle). We presumed in our model a first crystallization of volatile-free pheno-crystals of Bg, followed by a simultaneous eutectic crystallization of Fpc and Bg in volumetric ratios of 25:75 ([Baron et al., 2017](#)).

We estimated the relative abundance ratios of NGs (only stable isotopes normalized to Ar) retained in the solid LM using the solubilities extracted from the LSM (**Figure 7**). We compared the calculated normalized NG abundance patterns in the solid LM to those reported by [Marty \(2012\)](#) for the bulk mantle that are obtained by a global mass balance approach of

radiogenic ^{40}Ar . We also compared them to those given by [Moreira and Kurz \(2013\)](#) which were evaluated from ^3He abundances in OIBs. The results are presented in **Figure 8a** for an initial NG MO composition similar to phase Q and an additional solar contribution of 10% for Ne and Ar as suggested by [Marty \(2012\)](#). Our estimated Ne/Ar ratio in the solid LM is slightly larger than the one reported by [Moreira and Kurz \(2013\)](#) but one order of magnitude larger than the one obtained by [Marty \(2012\)](#). The estimated Kr/Ar and Xe/Ar ratios of the solid LM agree well with those evaluated by [Marty \(2012\)](#). This suggests (especially for heavy NGs) that the solid LM could represent a deep NG reservoir that is not readily sampled by plumes.

4.3. NG replenishment from the LM to the atmosphere

In the following, we discuss the contribution of NG replenishment from the LM through partial melting and plume volcanism to the present-day atmosphere over geological times. Stable Ne isotopes reveal that the present-day atmosphere has lost most of its primordial solar-like signature. This might be due to the moon-forming impact (MFI) that occurred 40-60 Myrs after Earth formation and that induced a massive erosion of primordial volatiles from the atmosphere and from the MO generated by the impact. One plausible scenario suggests that the impactor's (potentially Q-like) NG signature may have led to an overprint of the residual NGs. The ^{129}Xe abundances estimated from the $^{129}\text{I}/^{127}\text{I}$ ratio systematically constrain the loss of ^{129}Xe on Earth to 97% ([Avice and Marty, 2014](#); [Schlichting and Mukhopadhyay, 2018](#); and references therein).

Xe isotopic compositions also imply that most of present-day atmospheric NGs might have been acquired during late accretion of chondritic and cometary materials. This is related to the origin of atmospheric Xe that is most likely cometary U-Xe ([Avice et al, 2017](#); [Marty et al., 2017](#)). Such relatively small impacts may have not induced a re-melting and re-homogenization of the mantle but may have modified the atmospheric NG signature relatively to the one in the MORB and OIB sources. Overall, this suggests that replenishment of LM NGs

has not played a major role for the composition of the present-day atmosphere (Tieloff et al., 2000).

In the following, we evaluate the maximum contribution of replenished LM NGs to the present-day atmosphere. To this aim, we considered an extreme scenario which assumes that only the solid LM has captured solar-wind like Ne after the MFI and that the solar-like signature in the present-day atmosphere is entirely due to LM replenishment (**Supplementary Information**).

In this model, we considered an atmosphere of the Early Earth with chondritic NG abundances that has lost its primordial solar signature during the giant impact phase of planetary accretion. We took into account the element mass fractionation and volatile loss (no isotope fractionation) due to the impact that affect lighter NGs to a larger extend. Due to the lack of data on the effect of the impact loss for all NGs, we scaled the losses of Kr, Ar and Ne to the one of Xe (75%) (Schlichting and Mukhopadhyay, 2018) using the relations reported by Pepin (1997) for hydrodynamic escapes. This leads to residual fractions of: 25% Xe, 10% Kr, 1.3% Ar and 0.7% Ne. We obtained an atmospheric Neon-B component of 30.4% and a remaining 68.9% cometary and chondritic contributions (see Supplementary Information for details). From the analysis of refractory comet grains, Marty et al. (2008) established that the cometary contribution could be Q-like. This was also assumed in our model. For Xe, an additional loss of 22% was considered to account for the progressive isotope fractionation due to the ionization of dominantly light Xe isotopes by enhanced EUV flux from the young sun (Avice et al., 2017).

The resulting modelled normalized NG abundances in the atmosphere are shown in **Figure 8b**. The obtained Kr/Ar and Xe/Ar ratios are close to those of the present-day atmosphere. The modelled Ne/Ar ratio is however much lower than the present-day one. In order to increase the Ne/Ar ratio, it is necessary to include solar contributions because the

Ne/Ar ratios of the LM, comets and chondrites are below the atmospheric ratio. A solar-like Ne/Ar ratio could originate from the outgassing of the Earth's core or could have been captured in the early atmosphere due to solar-wind irradiation. The required addition of a high solar-like Ne/Ar ratio from another reservoir implies a significantly lower contribution of LM NGs to the present-day atmosphere. This conclusion is consistent with the study of Holland et al. (2009) in which they found that Kr and Xe play only a minor role in determining the NG composition of the modern atmosphere. All these arguments thus suggest that the LM may not be fully outgassed and could be an available NG reservoir through geologic times.

Acknowledgements

We thank the reviewers for their constructive comments that helped improve the manuscript. We also greatly appreciated the way the editor handled it. We thank the ESRF for allocating beamtime to this project, I. Kantor, R. Torchio and S. Boccato for their help in setting up the experiments, F. Perrin, S. Pasternak, J.-L. Devidal and J. Jacobs for technical assistance. MAB acknowledges the support of the Labex ClerVolc (This is laboratory of Excellence ClerVolc contribution number xxxx).

References

- Allègre, C.J., Staudacher, T., Sarda, P., Kurz, M., 1983. Constraints on evolution of Earth's mantle from rare gas systematics. *Nature* 303, 762–766, DOI: <https://doi.org/10.1038/303762a0>.
- Allègre, C.J., Turcotte, D., 1986. Implications for a two-component marble-cake mantle. *Nature*, 323, 123-127, DOI: <https://doi.org/10.1038/323123a0>.
- Auzende, A.-L., Badro, J., Ryerson, F.J., Weber, P.K., Fallon, S.J., Addad, A., Siebert, J., Fiquet, G., 2008. Element partitioning between magnesium silicate perovskite and

545 ferropericlasite: New insights into bulk lower-mantle geochemistry. *Earth Planet. Sci. Lett.*,
 546 269, 164-174. DOI: <https://doi.org/10.1016/j.epsl.2008.02.001>.
 547 Avice, G., Marty, B., 2014. The iodine-plutonium-xenon age of the Moon–Earth system
 548 revisited. *Philos. Trans. R. Soc. Lond. Ser. A, Math. Phys. Sci.* 372, 20130260. DOI:
 549 <https://doi.org/10.1098/rsta.2013.0260>.
 550 Avice, G., Marty, B., Burgess, R., 2017. The origin and degassing history of the Earth's
 551 atmosphere revealed by Archean xenon. *Nature Com.*, 8:15455, 1-9. DOI:
 552 <https://doi.org/10.1038/ncomms15455>.
 553 Baron, M., Lord, O., Myhill, R., Thomson, A. R., Wang, W. Tronnes, R.G., Walter, M.J., 2017.
 554 Experimental constraints on melting temperatures in the MgO–SiO₂ system at lower mantle
 555 pressures. *Earth Planet. Sci. Lett.*, 472, 186-196, DOI:
 556 <https://doi.org/10.1016/j.epsl.2017.05.020>.
 557 Blundy, J., Wood, B., 2003. Partitioning of trace elements between crystals and melts. *Earth*
 558 *Planet. Sci. Lett.*, 210, 383-397, DOI: [https://doi.org/10.1016/S0012-821X\(03\)00129-8](https://doi.org/10.1016/S0012-821X(03)00129-8).
 559 Bouhifd, M.A., Jephcoat, A.P., Heber, V.S., Kelley, S.P., 2013. Helium in the Early Earth core.
 560 *Nat. Geosci.*, 6, 982-986, DOI: <https://doi.org/10.1038/ngeo1959>.
 561 Bouhifd, M.A., Jephcoat, A.P., 2006. Aluminium control of argon solubility in silicate melts
 562 under pressure. *Nature*, 439, 961-964, DOI: <https://doi.org/10.1038/nature04583>.
 563 Brooker, R.A., Du, Z., Blundy, D.J., Kelley, S.P., Allan, N.L., Wood, B.J., Chamorro, E.M.,
 564 Wartho, J.A., Purton, J.A., 2003. The 'zero charge' partitioning behaviour of noble gases
 565 during mantle melting. *Nature*, 423, 738–741, DOI: <https://doi.org/10.1038/nature01708>.
 566 Campbell, A.J., 2008. Measurement of temperature distributions across laser heated samples
 567 by multispectral imaging radiometry. *Rev. Sci. Instrum.*, 79, 015108, DOI:
 568 <https://doi.org/10.1063/1.2827513>.

569 Carroll, M.R., Stolper, E.M., 1993. Noble gas solubilities in silicate melts and glasses: New
 570 experimental results for argon and the relationship between solubility and ionic porosity.
 571 *Geochim. Cosmochim. Ac.*, 57, 5039–5051, DOI: [https://doi.org/10.1016/0016-](https://doi.org/10.1016/0016-7037(93)90606-W)
 572 7037(93)90606-W.

573 Chamorro-Perez, E., Gillet, P., Jambon, A., 1996. Argon solubility in silicate melts at very high
 574 pressures. Experimental set-up and preliminary results for silica and anorthite melts. *Earth*
 575 *Planet. Sci. Lett.*, 145, 97–107, DOI: [https://doi.org/10.1016/S0012-821X\(96\)00188-4](https://doi.org/10.1016/S0012-821X(96)00188-4).

576 Du, Z., Lee, K.M., 2014. High-pressure melting of MgO from (Mg,Fe)O solid solutions.
 577 *Geophys. Res. Lett.*, 41, 8061 – 8066, DOI: <https://doi.org/10.1002/2014GL061954>.

578 Fischer, R. A., Langenhorst, F., Nakajima, Y., Campbell, A.J., Forst, D.J. Falko, D. H.,
 579 Miyajima, N. Pollok, K., Rubie, D., 2015. High pressure metal–silicate partitioning of Ni,
 580 Co, V, Cr, Si, and O. *Geochim. Cosmochim. Ac.*, 167, 177–194. DOI:
 581 <https://doi.org/10.1016/j.gca.2015.06.026>.

582 Heber, V.S., Brooker, R.A., Kelley, S.P., Wood, B.J., 2007. Crystal-melt partitioning of noble
 583 gases (helium, neon, argon, krypton, and xenon) for olivine and clinopyroxene. *Geochimica*
 584 *Cosmochimica Acta*, 71, 1041–1061, DOI: <https://doi.org/10.1016/j.gca.2006.11.010>.

585 Hofman, A.W., Hart, S.R., 1978. An assessment of local and regional isotopic equilibration in
 586 the mantle. *Earth Planet. Sci. Lett.*, 38, 44-62, DOI: [https://doi.org/10.1016/0012-](https://doi.org/10.1016/0012-821X(78)90125-5)
 587 821X(78)90125-5.

588 Holland G., Cassidy M., Ballentine C.J., 2009. Meteorite Kr in Earth’s mantle suggests a late
 589 accretionary source for the atmosphere. *Science* 326, 1522-1525, DOI:
 590 <https://doi.org/10.1126/science.1179518>.

591 Jackson, C.R.M., Parman, S.W., Kelley, S.P., Cooper, R.F., 2013. Noble gas transport into the
 592 mantle facilitated by high solubility in amphibole. *Nat. Geosci.* 6, 562-565, DOI:
 593 <https://doi.org/10.1038/ngeo1851>.

594 Jephcoat, A.P., 1998. Rare-gas solids in the Earth's deep interior. *Nature* 393, 355-358, DOI:
595 <https://doi.org/10.1038/30712>.

596 Kantor, I, Dubrovinsky, L., McCammon, C., Steinle-Neumann, G., Kantor, A., 2009. Short-
597 range order and Fe clustering in $\text{Mg}_{1-x}\text{Fe}_x\text{O}$ under high pressure. *Physical Rev. B*, 80,
598 014204, DOI: <https://doi.org/10.1103/PhysRevB.80.014204>.

599 Karato, S-I., 2016. Physical basis of trace element partitioning: A review. *Am. Mineral.*, 101,
600 2577-2593, DOI: <https://doi.org/10.2138/am-2016-5665>.

601 Labrosse, J.W., Hernlund, N., Coltice, A., 2007. A crystallizing dense magma ocean at the base
602 of the Earth's mantle. *Nature*, 450, 866–869, DOI: <https://doi.org/10.1038/nature06355>.

603 Lord, O.T., Wood, I. G., Dobson, D. P., Vočadlo, L., Wang, W. Thomson, A. R., Wann, E.T.H.,
604 Morard, G., Mezouar, M., Walter, M.J., 2014. The melting curve of Ni to 1 Mbar. *Earth*
605 *Planet. Sci. Lett.*, 408, 2014, 226-236, DOI: <https://doi.org/10.1016/j.epsl.2014.09.046>.

606 Martin, P.M., Vathonne, E., Carlot, G., Delorme, R., Sabathier, C., Freyss, M., Garcia, P.,
607 Bertolus, M., Glatzel, P., Proux, O., 2015. Behavior of fission gases in nuclear fuel: XAS
608 characterization of Kr in UO_2 . *J. Nucl. Mater.*, 466, 379-392, DOI:
609 <https://doi.org/10.1016/j.jnucmat.2015.08.019>.

610 Marty, B., Altwegg, K., Balsiger, H., Bar-Nun, A., Bekaert, D.V., Berthelier, J.-J., Bieler, A.,
611 Briois, C., Calmonte, U., Combi, M., De Keyser, J., Fiethe, B., Fuselier, S.A., Gasc, S.,
612 Gombosi, T.I., Hansen, K.C., Hässig, M., Jäckel, A., Kopp, E., Korth, A., Le Roy, L., Mall,
613 U., Mousis, O., Owen, T., Rème, H., Rubin, M., Sémon, T., Tzou, C.-Y., Waite, J.H.,
614 Wurz., P., 2017. Xenon isotopes in 67P/Churyumov-Gerasimenko show that comets
615 contributed to Earth's atmosphere. *Science*, 356, 6342, 1069-1072, DOI:
616 <https://doi.org/10.1126/science.aal3496>.

617 Marty, B., 2012. The origins and concentrations of water, carbon, nitrogen and noble gases on
 618 Earth. *Earth Planet. Sci. Lett.*, 313-314, 56-66, DOI:
 619 <https://doi.org/10.1016/j.epsl.2011.10.040>.
 620 Marty, B., Palma, R.L., Pepin, R.O., Zimmermann, L., Schlutter, D.J., Burnard, P., Westphal,
 621 A.J., 2008. Helium and Neon abundances and compositions in cometary matter. *Science*,
 622 319, 75-78, DOI: <https://doi.org/10.1126/science.1148001>.
 623 Matsuda, J., Sudo, M., Ozima, M., Ito, K., Ohtaka, O., Ito, E., 1993. Noble gas partitioning
 624 between metal and silicate under pressure. *Science*, 259, 788-90, DOI:
 625 <https://doi.org/10.1126/science.259.5096.788>
 626 Morard, G., Andrault, D., Guignot, N., Sanloup, C., Mezouar, M., Petitgirard, S., Fiquet G.,
 627 2008. In situ determination of Fe–Fe₃S phase diagram and liquid structural properties up to
 628 65 GPa. *Earth Planet. Sci. Lett.*, 272, 620–626, DOI:
 629 <https://doi.org/10.1016/j.epsl.2008.05.028>.
 630 Morard, G., Andrault, D., Guignot, N., Siebert, J., Garbarino, G., Antonangeli, D., 2011.
 631 Melting of Fe–Ni–Si and Fe–Ni–S alloys at megabar pressures: implications for the core–
 632 mantle boundary temperature. *Phys. Chem. Min.*, 38, 767–776. DOI:
 633 <https://doi.org/10.1007/s00269-011-0449-9>.
 634 Moreira, M., 2013. Noble gas constrains on the origin and evolution of the Earth's volatiles.
 635 *Geochem. Perspect.*, 2, 229-403.
 636 Moreira, M., Kurz, M.D. 2013. Noble gases as tracers of mantle processes and magmatic
 637 degassing. Chapter 12. In: *Advances in Isotope Geochemistry* (Ed: P. Burnard). Recherche
 638 Scientifique, Centre de Recherches Pétrographiques et Centre National de laVandoeuvre-
 639 lès-Nancy France. DOI : DOI https://doi.org/10.1007/978-3-642-28836-4_12

640 Mori, Y., Ozawa, H., Hirose, K., Sinmyo, R., Tateno, S., Morard, G., Ohishi, Y., 2017. Melting
641 experiments on Fe–Fe₃S system to 254 GPa. *Earth Planet. Sci. Lett.*, 464, 135–141. DOI:
642 <https://doi.org/10.1016/j.epsl.2017.02.021>.

643 Mukhopadhyay, S., 2012. Early differentiation and volatile accretion recorded in deep mantle
644 neon and xenon. *Nature*, 486, 101-104, DOI: <https://doi.org/10.1038/nature11141>.

645 Niwa, K., Miyakawa, C., Yagi, T., Matsuda, J.-i., 2013. Argon solubility in SiO₂ melt under
646 high pressures: A new experimental result using laser-heated diamond anvil cell. *Earth*
647 *Planet. Sci. Lett.*, 363, 1, 1-8, DOI: <https://doi.org/10.1016/j.epsl.2012.12.014>.

648 Noordhuis, J., De Hosson, J. Th.M., 1991. Fundamental and applied aspects of noble gas
649 bubbles in steel. Edited by S.E. Donnelly and J.H. Evans. Plenum Press. New York, p. 153-
650 165, DOI: https://doi.org/10.1007/978-1-4899-3680-6_13.

651 Norton, M.G, Carter, C.B., Fleischer, E., Mayer, J.W., 1992. Solid krypton in MgO. *J. Mat.*
652 *Res.*, 7, 12, DOI: <https://doi.org/10.1557/JMR.1992.3171>.

653 Pepin, R. O., Porcelli, D., 2006. Xenon isotope systematics, giant impacts, and mantle
654 degassing on the early Earth. *Earth Planet. Sci. Lett.*, 250 (3-4), 470-485, DOI:
655 <https://doi.org/10.1016/j.epsl.2006.08.014>.

656 Pepin, R. O., Porcelli, D., 2002. Origin of noble gases in the terrestrial planets. *Rev. Mineral.*
657 *Geochem.*, 47, 191–246, DOI: <https://doi.org/10.2138/rmg.2002.47.7>.

658 Pepin, R.O., 1997. Evolution of Earth's noble gases: consequences of assuming hydrodynamic
659 loss driven by giant impact. *Icarus*, 126, 148-156, DOI:
660 <https://doi.org/10.1006/icar.1996.5639>.

661 Rosa, A.D., Garbarino, G., Briggs, R., Svitlyk, V., Morard, G., Bouhifd, M.A., Jacobs, J.,
662 Irifune, T., Mathon, O., Pascarelli, S., 2018. Effect of the fcc-hcp martensitic transition on
663 the equation of state of solid krypton up to 140 GPa. *Physical Rev. B*, 97, 094115. DOI:
664 <https://doi.org/10.1103/PhysRevB.97.094115>.

665 Rubie D. C., Frost D. J., Mann U., Asahara Y., Nimmo F., Tsuno K., Kegler P., Holzheid A.,
 666 Palme, H., 2011. Heterogeneous accretion, composition and core–mantle differentiation of
 667 the Earth. *Earth Planet. Sci. Lett.*, 301, 31–42, DOI:
 668 <https://doi.org/10.1016/j.epsl.2010.11.030>.
 669 Schlichting, H. E., Mukhopadhyay, S., 2018. Atmosphere impact losses. *Space Sci. Rev.*,
 670 214:34, 1–31, DOI: <https://doi.org/10.1007/s11214-018-0471-z>.
 671 Shcheka, S.S., Keppler, H., 2012. The origin of the terrestrial noble-gas signature. *Nature*, 490,
 672 531–534, DOI: <https://doi.org/10.1038/nature11506>.
 673 Solomatov, V.S., Stevenson, D.J., 1993. Nonfractional crystallization of a terrestrial magma
 674 ocean. *J. Geophys. Res.* 98, 5391–5406. DOI: <https://doi.org/10.1029/92JE02579>.
 675 Tan, Z. Budnick, J.I., Pease, D.M., Namavar, F., 1991. X-ray absorption of krypton precipitates
 676 in solid matrices. *Phys. Rev. B*, 43, 3, 1987–1992, DOI:
 677 <https://doi.org/10.1103/physrevb.43.1987>.
 678 Tieloff, M., Kunz, J., Clague, D.A., Harrison, D., Allègre, C.J., 2000. The nature of pristine
 679 noble gases in mantle plumes. *Science* 288, 1036–1039. DOI:
 680 <https://doi.org/10.1126/science.288.5468.1036>
 681 Watson, E.B., Thomas J.B., Cherniak, D.J., 2007. ⁴⁰Ar retention in the terrestrial planets.
 682 *Nature*, 449, 299–304. DOI: <https://doi.org/10.1038/nature06144>
 683 Zhang, Y., Zhu., X., 1995. Atomic radii of noble gas elements in condensed phases. *Am. Min.*,
 684 80, 670–675, DOI: <https://doi.org/10.2138/am-1995-7-807>.

Figures and Tables

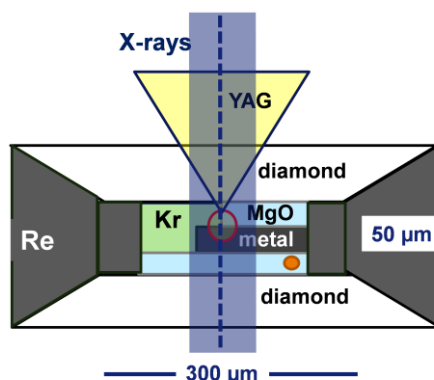


Figure 1. Schematic view of a typical diamond anvil cell sample loading (Cell_2, **Table 1** and **Figure S1**) designed for the present experiments. A diamond culet size of 300 μm allows reaching 60 GPa. A metal foil (gray) is sandwiched between two MgO pellets (light blue). On the laser-heated side, the metal foil is not fully covered by MgO. The remaining sample chamber was filled with supercritical Kr (250 bars). For the partitioning experiments, the sample was heated on one side at the contact surface of the three materials. In the experiments carried out up to 60 GPa, the laser was slightly defocused (yellow triangle) to provide a larger laser spot size of approximately 40-60 μm in diameter. At the K-edge energy of Kr (14.3 keV) the focused X-ray beam (blue dashed line) exhibited large tails of ~ 50 μm at full width half maximum adjacent to the focused X-ray beam (blue shaded area). These tails arise from the deep penetration of the X-ray beam in the bended polychromatic Si(111) crystal used for horizontal focusing. This effect becomes significant for X-ray beam energies above 10 keV.

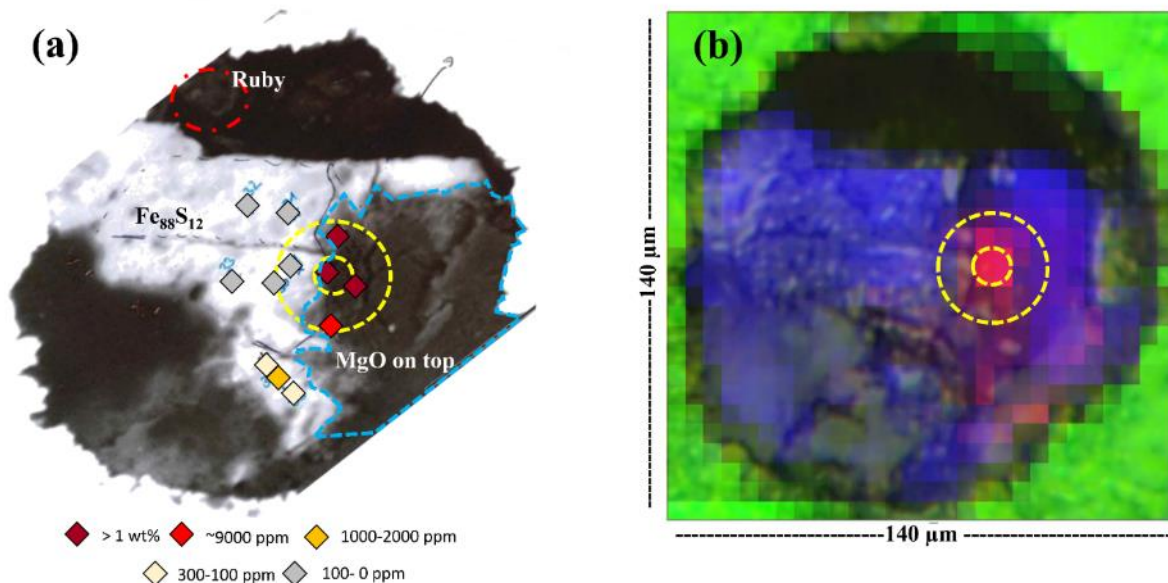
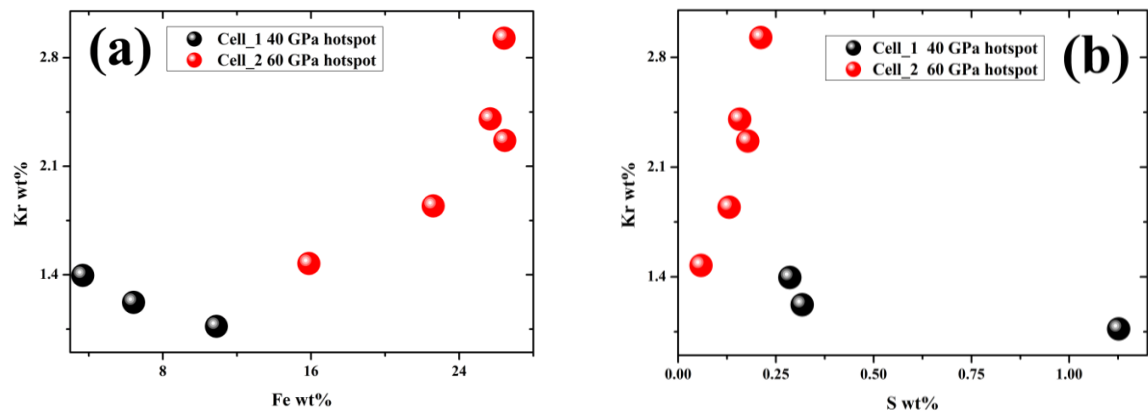


Figure 2. (a) Back scattered electron image of the sample Cell_1 (Table 1). The diamond symbols indicate the positions of EMPA measurements (Table S1), the symbol colors scale with the measured Kr concentrations in each point as given in the legend below the figure. The position of the ruby sphere and MgO pellet (Fpc in the heating spot) placed next to and on top of the Fe-S-alloy are outlined by a red circle and a blue dashed line, respectively. (b) Photograph of the same sample superimposed on the false color map of the μ XRF element distribution. The intensity of each color scales with the signal intensities of the corresponding XRF emission line of the element that is proportional to its concentration (green Re L_{α} , blue Fe K_{α} , and pink Kr K_{α}). Note that the MgO pellet cannot be observed in this figure because the Mg and O K_{α} emission lines are completely absorbed by the air volume located between the sample and the XRF detector. The yellow dashed circles delineate the positions of the central laser-heated hotspot (small circle with a diameter of 20 μ m) and the entire laser spot (big circle with a diameter of 40 μ m).

715



716 **Figure 3.** Measured Kr concentrations in Fpc after quenching of laser heated samples subjected
717 to 2300 K and 40 GPa (black circles) and 60 GPa (red circles) as a function of **(a)** the Fe content
718 and **(b)** the S content (in wt.%). Only data acquired in the center of the laser-heated hotspot
719 region (within a diameter of 20 μm) are shown (**Table 1** and **S1**). Uncertainties on the EMPA
720 measurements are within the symbol size for Kr and Fe (103 and 816 ppm, respectively). The
721 detection limits of S (642 ppm) exceed the measured quantities for most points and therefore
722 plot **(b)** can only be used for evaluating chemical trends.

723

724

725

726

727

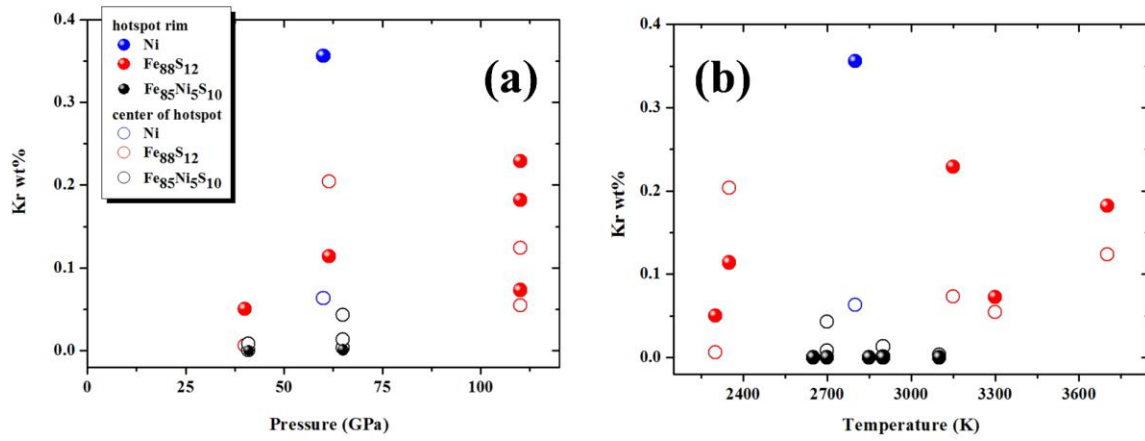


Figure 4. Averaged Kr concentrations in metallic melts with different compositions after quenching as a function of (a) pressure and (b) temperature. Open and filled symbols indicate the averaged data acquired in the central portion of the laser hotspot (within a diameter of 20 μm) and at the rim of the hotspot (within a diameter range of 20-40 μm), respectively.

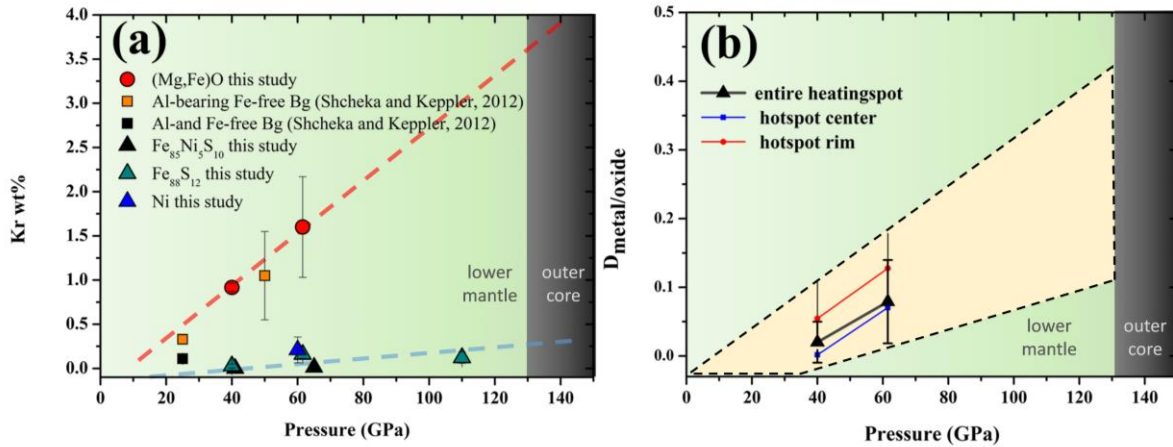


Figure 5 (a) Estimated maximal Kr solubilities in Fpc and metallic melts (red squares and black, blue and cyan triangles) as a function of pressure at 2300 K. The solubilities are obtained by averaging up to 10 individual measurements (Table 1 and S1). The extrapolation of solubility data to the core mantle boundary (CMB) conditions is delineated by red and cyan dashed lines for Fpc and Fe₈₈S₁₂, respectively. The results of the Kr solubility in Fe-free and Al-bearing bridgmanite (Bg) from Shcheka and Keppler (2012) are shown for comparison as black and orange squares. They have been experimentally determined at 25 GPa and 1800 K and estimated from lattice strain modelling at 50 GPa. (b) Approximated partitioning coefficient $D_{\text{metal/oxide}}$ between (Mg_{1-x},Fe_x)O and Fe₈₈S₁₂ for Kr as a function of pressure at 2300 K (Cell_1-3, Table 1). The black triangles, blue squares and red circles indicate the calculated D values using measurements from the entire heating spot (within a diameter of 40 μm), the central portion of the hotspot (within a diameter of 20 μm) and the outer rim of the hotspot (within a diameter range of 20-40 μm), respectively. The yellow shaded area indicates the extrapolation of the experimental $D_{\text{metal/oxide}}$ values to the Earth's outer core conditions and takes into account the uncertainties.

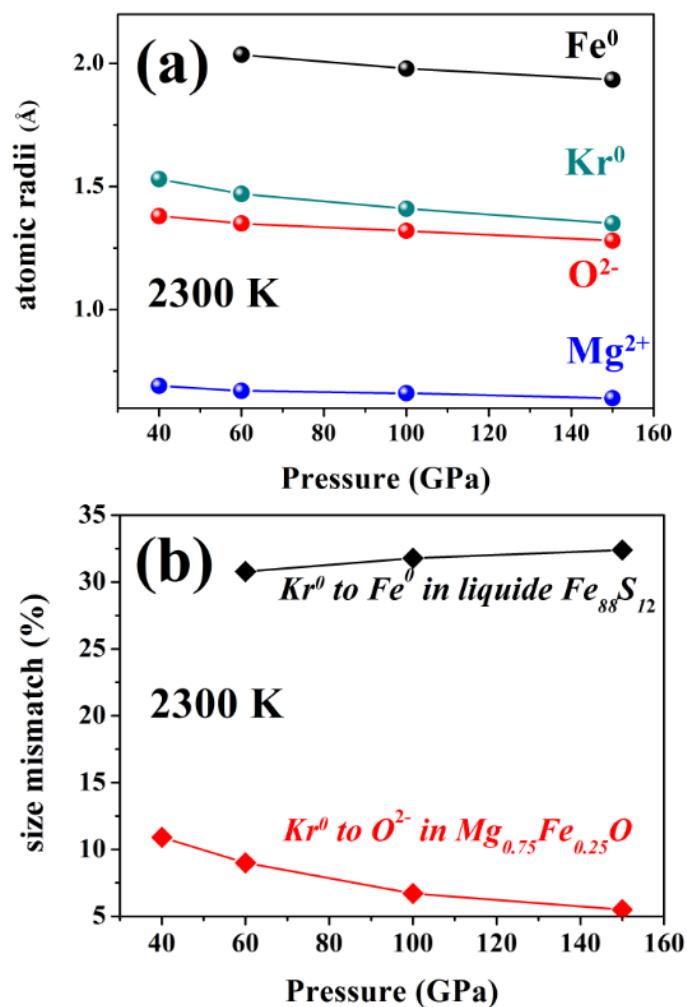


Figure 6 (a) Calculated atomic radii of zero-charged Kr⁰ in solid fcc Kr, Fe⁰ in liquid Fe₈₈S₂₂ and O²⁻ and Mg²⁺ in solid Mg_{0.75}Fe_{0.25}O as a function of pressure at 2300 K. The radii have been calculated using the thermal equation of states of the solids and density data of the liquids. (b) Evolution of the size mismatch (in %) with pressure at 2300 K between the radii of zero-charged Kr⁰ and oxygen vacancies in Mg_{0.75}Fe_{0.25}O (O²⁻) and vacant hard-sphere sites in Fe₈₈S₂₂ (Fe⁰) (See **Supplementary Information** for more details).

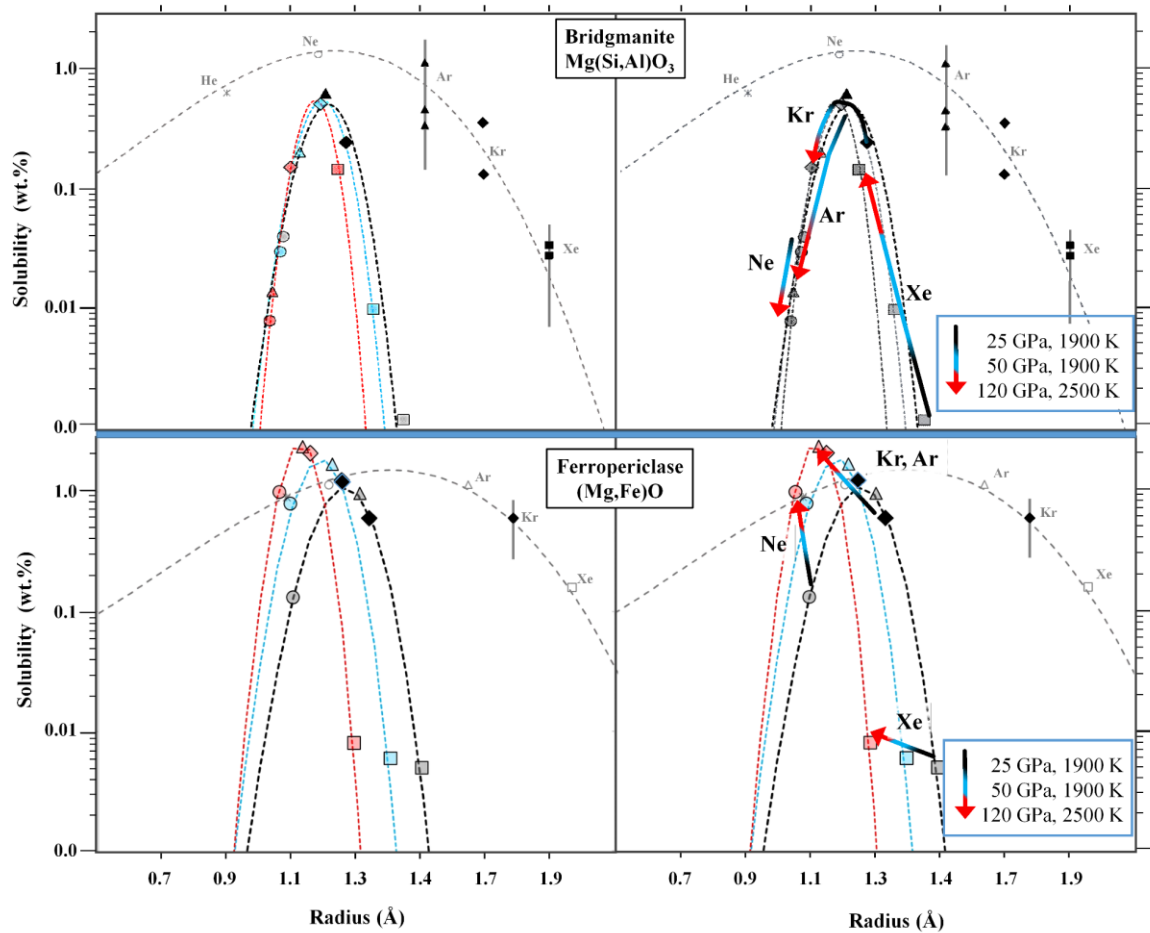


Figure 7. Left panels: Solubility trend versus NG radius in oxygen vacancies of Fe-free Al-bearing Bg ($\text{Mg}(\text{Al,Si})\text{O}_3$, top) and Fpc ($(\text{Mg,Fe})\text{O}$), bottom) at different P/T conditions obtained from lattice strain modelling (**Supplementary Information**), (gray: ambient; black: 25 GPa and 1900 K; blue: 50 GPa and 1900 K; red: 120 GPa and 2500 K). Squares: Xe; diamonds: Kr; triangles: Ar; circles: Ne; stars: He. Filled black symbols indicate the solubilities obtained experimentally in this study and by [Shcheka and Keppler \(2012\)](#), the uncertainties on the solubilities are represented by gray bars. The models obtained from the classical lattice strain approach (gray dashed lines) are compared to those obtained with the extended approach developed in this study (dotted colored lines). Note that in the classical approach the experimentally determined solubilities are fitted to ambient condition NG radii (r_i) by adjusting the host site flexibility (E_m), the maximum solubility of the site (c_0) and the host site radii (r_0).

In the extended approach r_i , r_0 and E_m are fixed to the calculated values derived from the thermoelastic data obtained at high P/T conditions. In this case, the only fitting parameter is c_0 . Right panels: NG solubility trends from the top to the bottom of the LM indicated by arrows (black to red). Note that the differences in NG and oxygen vacancy site radii at equivalent conditions for Fpc and Bg arise from the differences in coordination environments that is [6]-fold in Fpc and [4]-fold in Bg.

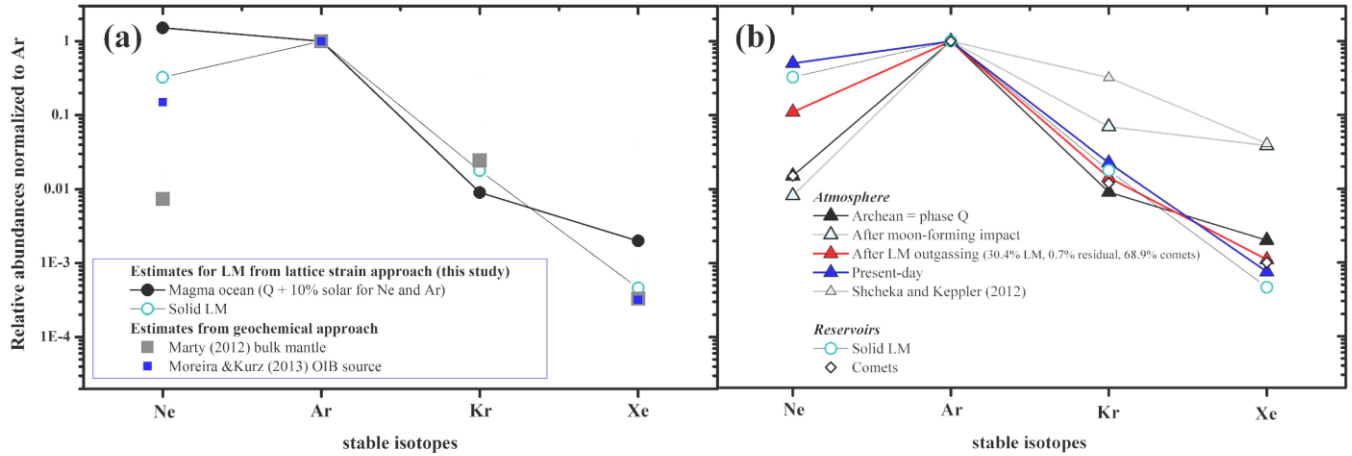


Figure 8. (a) Abundances of ^{20}Ne , ^{36}Ar , ^{84}Kr and ^{130}Xe (stable isotopes) normalized to ^{36}Ar dissolved in the magma ocean (MO, black circles) and retained in the solid mantle after MO crystallization (open circles) using the NG solubility data in LM minerals from **Figure 7**. Normalized abundances reported for the deep NG reservoir from [Marty \(2012\)](#) (gray squares) and [Moreira and Kurz \(2013\)](#) (blue squares) are shown for comparison. (b) Abundances of ^{20}Ne , ^{36}Ar , ^{84}Kr and ^{130}Xe normalized to ^{36}Ar in the Earth's atmosphere at different stages of its formation. It includes the abundances assumed for the Archean atmosphere (black triangles, phase Q-like), after elemental fractionation due to the moon forming impact (light blue triangles) and after NG re-injection from the LM Xe loss due to EUV irradiation and late-

787 veneer contribution (red triangles), present-day atmosphere (blue triangles) and abundances
788 after LM outgassing reported from [Shcheka and Keppler \(2012\)](#) (gray triangles). The
789 normalized NG abundances in different reservoirs are also shown, including the solid LM (blue
790 open circles), cometary ice (black open diamonds) and phase Q in chondrites which are
791 equivalent to those assumed in the present model for the Archean atmosphere (black triangles).

Table 1. Experimental runs conducted in this study sorted by loadings (Cell 1-7). We provide the following details: the number of laser-heated spots per loading, the insulating and starting material (KCl, MgO, metal foil composition), the experimental conditions for each laser-heated spot including the maximal pressure P in GPa (the errors correspond to the standard deviation of pressures measured before and after laser-heating) and temperature T in K (errors are of the order of 100-200 K). Kr concentrations from EMPA measurements in wt.% are given for the different phases (Fpc or metallic melts) and include averages of measurements acquired only in the hotspot center (center: within a diameter of 20 μm), only in the rim of the laser-heated spot (rim: with a diameter range of 20-40 μm from the center), in the entire hotspot region (everything: within a diameter of 40 μm) and the maximum Kr content measured in a single analysis (maximum). A detailed list of all measurements is provided in the **Supplementary Information Table S1**.

Run	LH-	Sample	P (GPa)	T (K)	Averaged Kr concentration** (wt.%)					
	spot				phase	center	rim	everything	maximum	
Kr metal/oxide partitioning										
Cell_1	1	MgO	Fe ₈₈ S ₁₂	40.0(5)	2300	(Mg _{1-x} ,Fe _x)O	1.23(13)	0.96(10)	1.16(16)	1.40(1)
		(b+t)*				Fe ₈₈ S ₁₂	0.0	0.05(2)	0.03(3)	0.11(1)
Cell_2	1	MgO	Fe ₈₈ S ₁₂	61.5(5)	2300	(Mg _{1-x} ,Fe _x)O	2.2(5)	0.99(4)	1.8(7)	2.93(1)
		(b+t)*				Fe ₈₈ S ₁₂	0.15(11)	0.13(5)	0.15(10)	0.39(1)
Kr incorporation into liquid/ solid metal foil										
	1				2700		0.05(8)	0.0	0.03(6)	0.14(1)
Cell_3	2	KCl (b)*	Fe ₈₃ Ni ₅ S ₁₂	65.0(5)	2900	Fe ₈₃ Ni ₅ S ₁₂	0.01(2)	0.0	0.01(1)	0.03(1)
	3				3100		0.0	0.0	0.0	0.0
Cell_4	1	KCl (b)*	Fe ₈₃ Ni ₅ S ₁₂	41(1)	2700	Fe ₈₃ Ni ₅ S ₁₂	0.0	0.08(1)	0.04(6)	0.08(1)
Cell_5	1	KCl (b)*	Ni	62.0(5)	2800	Ni	0.07(1)	0.37(26)	0.23(26)	0.77(1)
Cell_6	1				3150		0.08(1)	0.24(20)	0.14(13)	0.38(1)
	2	KCl (b)*	Fe ₈₈ S ₁₂	110(1)	3300	Fe ₈₈ S ₁₂	0.02(3)	0.06(6)	0.04(5)	0.14(1)
	3				3700		0.13(18)	0.18(21)	0.17(19)	0.38(1)
Cell_7	1	KCl (b)*	Fe ₈₈ S ₁₂	115(1)	1900	no EMPA				
	2	KCl (b)*			3100	no EMPA				

* Note: b and t denoted bottom and top, respectively.

** Reported values are averaged from 3-17 measurements, see **Table S1** of the **Supplementary Information**.

Supplementary Information

Krypton storage capacity of the Earth's lower mantle

A.D. Rosa¹, M.A. Bouhifd², G. Morard³, R. Briggs⁴, G. Garbarino¹, T. Irifune⁵,

O. Mathon¹, S. Pascarelli¹

⁶ *European Synchrotron Radiation Facility (ESRF), 71, Avenue des Martyrs, Grenoble, France.*

⁷ *Laboratoire Magmas et Volcans, Université Clermont Auvergne, CNRS, IRD, OPGC, F-63000 Clermont-Ferrand, France.*

⁸ *Sorbonne Université, Muséum National d'Histoire Naturelle, UMR CNRS 7590, IRD, Institut de Minéralogie, de Physique des Matériaux et de Cosmochimie, IMPMC, 75005 Paris, France.*

⁹ *Lawrence Livermore National Laboratory, Livermore, CA, United States of America*

¹⁰ *Geodynamics Research Center, Ehime University, 2-5 Bunkyo-cho, Matsuyama 790-8577, Japan*

Supplementary Information

816	Contents	Page
817	1. Laser-heating experiments at ID24.....	3
818	2. XRF experiments at BM23.....	3
819	3. EMPA calibration and measurement results.....	6
820	4. Size mismatch calculations.....	8
821	5. Kr incorporation in quenched samples from X-ray absorption data.....	8
822	6. Lattice strain model approach and parameters.....	14
823	7. Formation of volatile saturated liquid/melt phase during magma ocean crystallization.....	16
824	8. NG replenishment model and considered isotopic Ne signatures therein.....	16
825	9. References.....	17

Supplementary Information

1. Laser-heating experiments at ID24

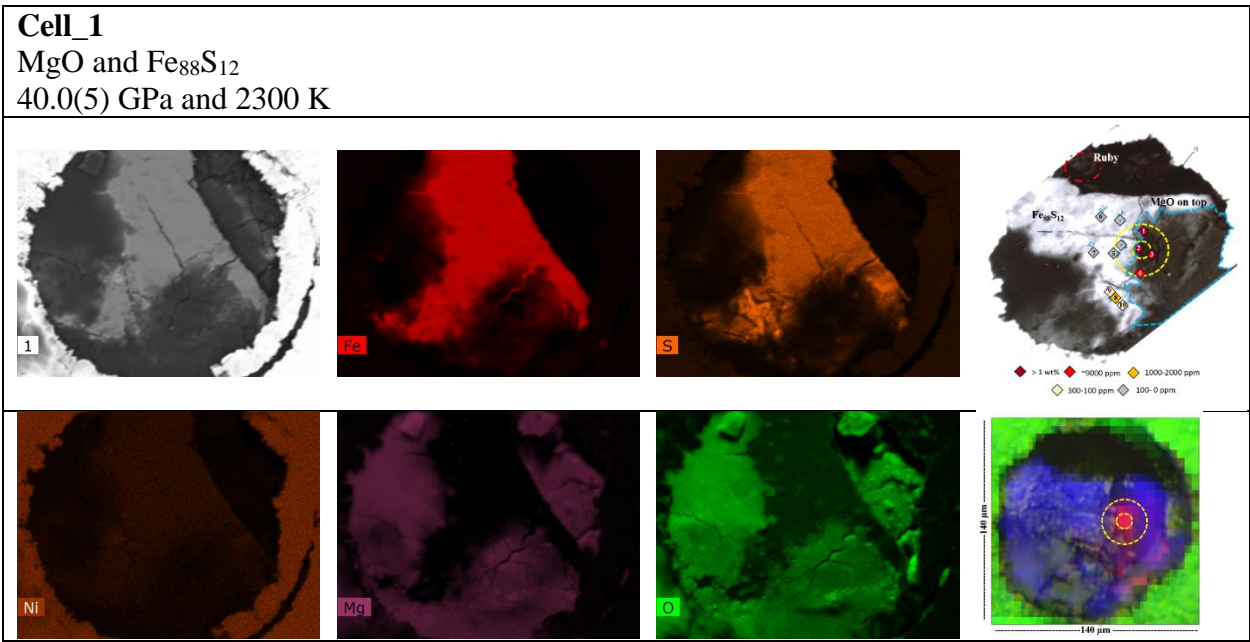
The samples were single-sided laser-heated using the laser-heating system installed at ID24 (Pascarelli et al., 2016; Kantor et al., 2018). The temperature was determined *in-situ* via spectroradiometry (Giampaoli et al., 2018). The pressure was measured before and after laser-heating using the ruby fluorescence signal and the ruby pressure scale after Dewaele et al. (2008) or the Raman shift of the single-crystal diamonds at the centre of the culet (Akawama and Kawamura, 2004).

2. XRF experiments at BM23

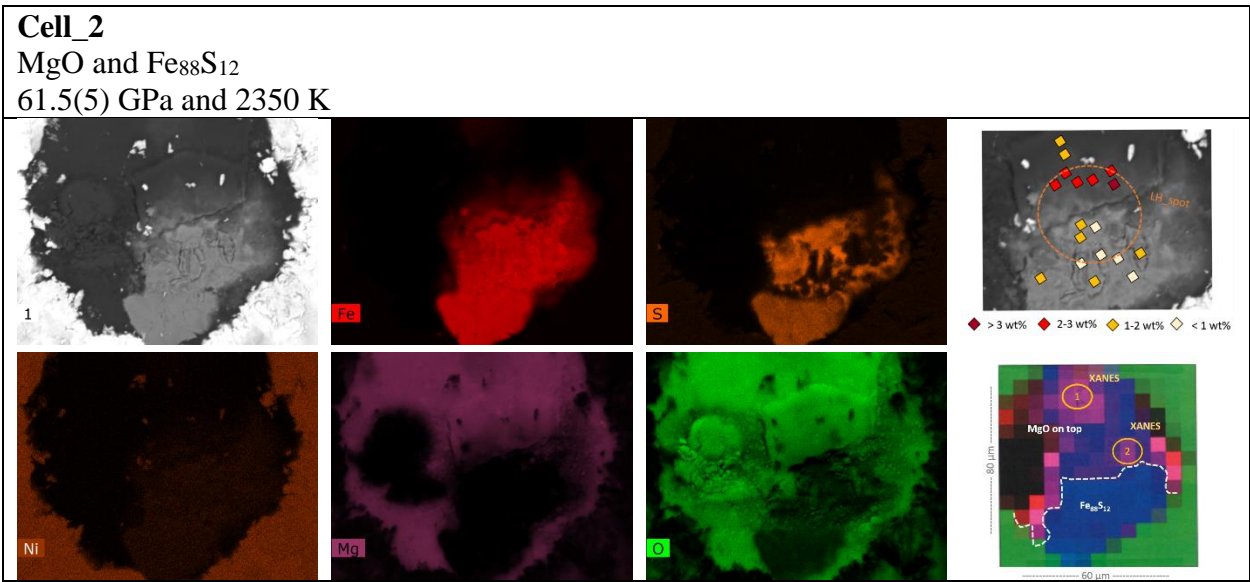
The X-ray energy was tuned to the Kr K-edge (14.2 keV) using a double-crystal fixed exit monochromator equipped with a pair of Si(111) crystals. The X-ray beam was focused down to $5 \times 5 \mu\text{m}^2$ using a KirkPatrick-Baez mirror system (Mathon et al., 2015). The quenched samples were oriented with the laser-heated surfaces towards the incoming X-ray beam. In order to avoid shadowing of the Re gasket, the samples were rotated by 15° from the incoming X-ray beam and towards the single-element **silicon** solid-state fluorescence detector (Vortex). The Vortex detector was positioned in backscattering geometry (rotated by 30° from the incoming X-ray beam).

In a first step, finely-meshed two-dimensional μXRF elemental distribution maps at a fixed X-ray energy of 14.5 keV were acquired for each sample with a step size of $5 \mu\text{m}$. These maps enabled determining the Kr distribution around the laser-heating spot (**Figure S1**). In a second step, X-ray absorption spectra were collected in regions of high Kr concentrations by scanning the monochromator energy with a small mesh size of energy points (0.4 eV) around the edge region and up to a k-range of 14 \AA^{-1} , respectively (**Figure S3 and S4**).

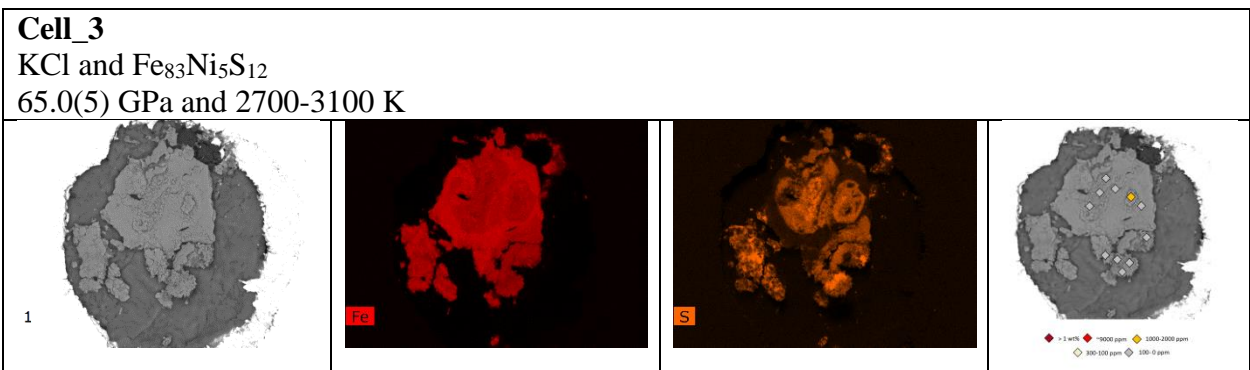
848



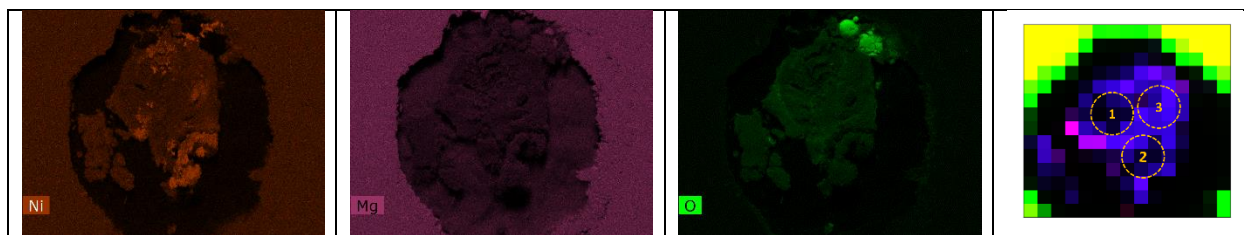
849



850



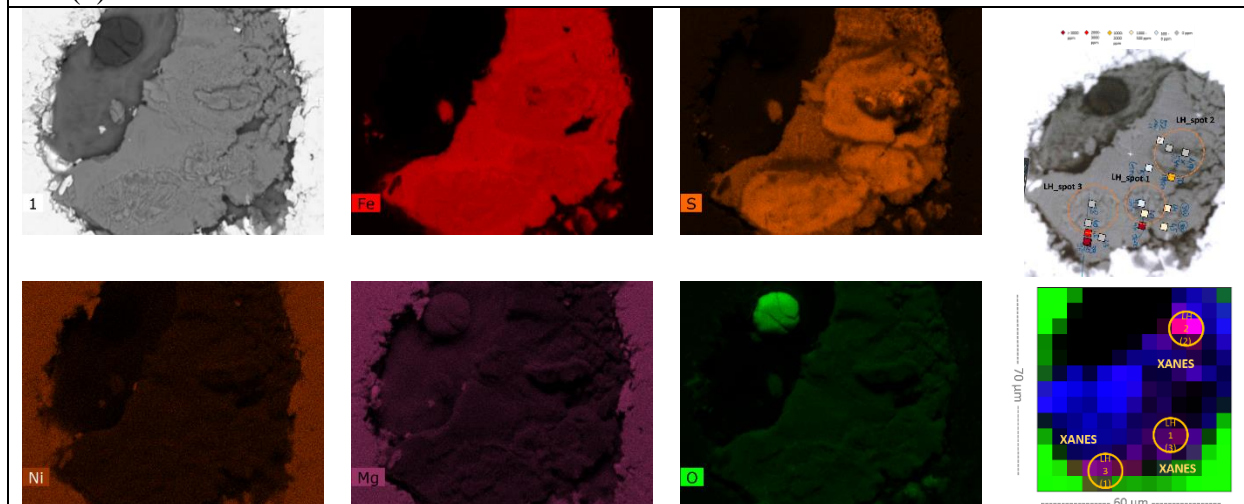
Supplementary Information



Cell_6

KCl and Fe₈₈S₁₂

110(1) GPa and 3150-3700 K



Cell_7

KCl and Fe₈₈S₁₂

115(1) GPa and 1900-3100 K

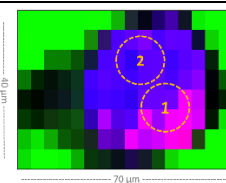


Figure S1. SEM, EMPA and μ XRF maps acquired on samples Cell_1, _2, _3, _6 and _7 (Table 1, main manuscript and Table S1). The figures for each sample include a raw back scattered electron (BSE) image and the corresponding elemental distribution maps of Fe (red), S (orange), Ni (brown), Mg (pink) and O (green). The **positions of acquired** EMPA measurements are outlined as diamond symbols in a **detailed BSE** image on the right. The coloured symbols indicate the measured concentration of Kr as outlined in the legend below the **detailed BSE** images. The position of the laser spot is delineated in the **detailed BSE** images as yellow circles having an inner circle representing the central hot-spot region. The XRF image is shown on the right below the detailed BSE image. It represents the elemental distribution of Kr in red; Fe in blue and O in green. The colour intensity scales with the abundance of the element. The sample size is given on the μ XRF image. Solid orange circles indicate the positions where X-ray absorption data were acquired.

Supplementary Information

3. EMPA calibration and measurement results

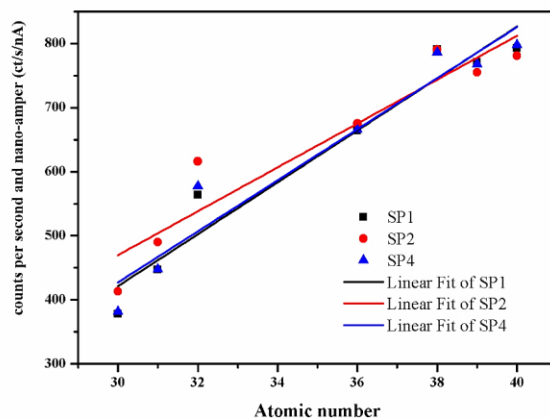


Figure S2. The EMPA Kr counts to concentration calibration using 7 standards of elements adjacent to Kr (from atomic number 30 to 40) for the three crystal detectors SP1, SP2 and SP3. Linear fits to the data are shown as solid lines.

Supplementary Information

Table S1. EMPA concentration measurements (in wt.%) and their distance from the centre of the laser heating spot. Averaged detection limits of elements are 530 ppm for Mg, 642 ppm for S, 816 ppm for Fe, 971 ppm for Ni and 103 ppm for Kr. Errors on temperature are in the order of 100-200 K.

Sample, LH-spot	Mg	S	Fe	Ni	Kr	P (Gpa)	T (K)	Distance from centre of hotspot
Cell_1, MgO	47.67	0.27	5.65	0	1.08	40.0(5)	2300	~10 μm
	47.25	1.07	10.34	0.08	1.01			~10 μm
	49.84	0.25	3.26	0.08	1.24			~10 μm
	49.19	0.35	2.35	0.02	0.18			10 -20 μm
Cell_1, Fe ₈₈ S ₁₂	0.07	9.36	89.27	0.09	0.00	40.0(5)	2300	~10 μm
	0.42	8.17	89.09	0.12	0.00			10 -20 μm
	0.14	8.50	90.11	0.17	0.00			10 -20 μm
	0.63	3.24	91.78	0.09	0.11			>20 μm
	0.17	13.1	84.04	0.08	0.03			>20 μm
	0.46	8.15	85.38	0.09	0.02			>20 μm
Cell_2, MgO	40.56	0.06	15.88	0.00	1.473	61.5(5)	2300	~10 μm
	35.23	0.21	26.43	0.02	2.9264			~10 μm
	41.21	0.13	22.59	0.01	1.8444			~10 μm
	38.64	0.16	25.67	0.01	2.4057			~10 μm
	38.51	0.18	26.46	0.03	2.266			~10 μm
	48.09	0.00	11.33	0.00	0.9489			10 -20 μm
	44.63	0.02	15.85	0.00	1.0297			10 -20 μm
Cell_2, Fe ₈₈ S ₁₂	0.17	11.80	87.71	0.23	0.09	61.5(5)	2300	< 10 μm
	0.25	10.37	88.79	0.20	0.39			< 10 μm
	0.07	13.38	86.31	0.17	0.07			~10 μm
	0.04	12.75	86.99	0.13	0.10			~10 μm
	0.02	2.87	96.94	0.12	0.05			~10 μm
	0.08	4.70	95.08	0.09	0.06			10 -20 μm
	0.09	4.12	95.56	0.09	0.14			10 -20 μm
	0.23	6.78	92.65	0.16	0.18			10 -20 μm
Cell_3, Fe ₈₃ Ni ₅ S ₁₂ , LH_1	0.00	12.96	78.17	8.87	0.00	65.0(5)	2700	< 10 μm
	0.00	7.67	82.49	9.70	0.14			< 10 μm
	0.01	13.04	78.97	7.98	0.00			~10 μm
	0.00	15.99	79.86	4.14	0.00			10 -20 μm
	0.00	11.89	84.73	3.38	0.00			10 -20 μm
Cell_3, Fe ₈₃ Ni ₅ S ₁₂ , LH_2	0.01	8.95	80.55	10.49	0.00			< 10 μm
	0.01	8.92	76.99	14.05	0.03			~10 μm
	0.04	5.25	80.55	14.15	0.01			~10 μm
	0.01	7.37	75.06	17.56	0.00			~10 μm
	0.00	10.71	78.91	10.37	0.00			10 -20 μm
Cell_3, Fe ₈₃ Ni ₅ S ₁₂ , LH_3	0.00	17.76	74.97	7.26	0.00	65.0(5)	3100	< 10 μm
	0.00	14.14	82.41	3.45	0.00			~10 μm
	0.02	15.17	81.53	3.26	0.01			~10 μm
	0.00	15.41	81.22	3.36	0.00			~10 μm
Cell_5, Ni, LH_1	0.02	0.02	0.02	99.91	0.03	62.0(5)	2800	< 10 μm
	0.00	0.03	0.03	99.92	0.02			< 10 μm
	0.01	0.00	0.01	99.97	0.01			< 10 μm
	0.01	0.00	0.02	99.93	0.04			< 10 μm
	0.03	0.00	0.00	99.95	0.03			< 10 μm
	0.00	0.00	0.02	99.77	0.21			10 -20 μm
	0.00	0.00	0.01	99.29	0.70			10 -20 μm
	0.00	0.02	0.01	99.62	0.35			10 -20 μm
	0.01	0.00	0.03	99.19	0.77			10 -20 μm
	0.01	0.01	0.00	99.81	0.17			10 -20 μm
	0.00	0.00	0.00	99.85	0.15			10 -20 μm
	0.01	0.01	0.03	99.68	0.26			10 -20 μm
Cell_6, Fe ₈₈ S ₁₂ , LH_1	0.00	9.43	90.41	0.08	0.08	110(1)	3150	< 10 μm
	0.00	7.60	92.18	0.14	0.07			< 10 μm
	0.00	10.29	89.53	0.11	0.07			~10 μm
	0.00	9.27	90.54	0.09	0.09			10 -20 μm
	0.00	5.98	93.58	0.06	0.38			10 -20 μm
Cell_6, Fe ₈₈ S ₁₂ , LH_2	0.00	11.21	88.54	0.25	0.00	110(1)	3300	< 10 μm
	0.01	9.13	90.60	0.25	0.01			< 10 μm
	0.03	8.37	91.41	0.13	0.06			< 10 μm
	0.02	11.45	88.27	0.12	0.14			~10 μm
	0.03	9.72	90.08	0.16	0.01			10 -20 μm
	0.00	8.53	91.36	0.09	0.02			10 -20 μm
Cell_6, Fe ₈₈ S ₁₂ , LH_3	0.00	15.08	84.80	0.12	0.00	110(1)	3700	< 10 μm
	0.00	15.25	84.41	0.08	0.25			~10 μm
	0.00	7.98	91.54	0.11	0.38			10 -20 μm
	0.02	13.44	86.37	0.18	0.00			10 -20 μm
	0.02	10.05	89.40	0.17	0.36			10 -20 μm
	0.01	14.49	85.40	0.10	0.00			10 -20 μm

882

883 **4. Size mismatch calculations**

884 Zero-charged Kr^0 atomic radii were calculated using the equation of state of fcc Kr
 885 determined by Rosa et al. (2018) and the assumed thermal parameters reported by Jephcoat (1998).
 886 For Fpc we calculated the anion and cation vacancy site radii using the thermal equation of state
 887 reported for $\text{Mg}_{0.75}\text{Fe}_{0.25}\text{O}$ by Mao et al. (2011) and an assumed bond ratio between Mg^{2+} and O^{2-}
 888 of 1/3 to 2/3, respectively. Such bond ratios are expected from the ion-radii values at ambient
 889 conditions (Zhang and Zhu, 1995). Average atomic radii for Fe^0 in the liquid were calculated using
 890 the density of liquid $\text{Fe}_{88}\text{S}_{12}$ reported from shock wave experiments at Earth's core conditions
 891 (Huang et al., 2013). For calculating the hard sphere diameter from the obtained densities, we used
 892 the Percus-Yevick equation assuming the arrangement of atoms in transition metal liquids can be
 893 described by the hard sphere model (Ashcroft and Lekner, 1966) with a packing fraction of 0.44
 894 as determined experimentally by Shen et al. (2004) for pure liquid iron. We further assumed a
 895 liquid structure consisting of zero-charged Fe^0 atoms with S atoms sitting in the interstitial sites as
 896 proposed by Posner et al. (2017).

897 **5. Kr incorporation in quenched samples**

898 Information on the local bonding environment of Kr retained in the samples can be
 899 obtained from X-ray absorption spectroscopy (XAS). XAS is a local and element selective probe,
 900 sensitive to the sort and arrangement of neighbouring atoms. Several energy regions in a XAS
 901 spectrum are distinguished: The white line energy corresponds to the ionization energy of the core
 902 electron and is defined as the energy position of the first peak in the spectrum's derivative function.
 903 The X-ray absorption near edge structure (XANES) region is defined in the energy domain
 904 between 50 and 100 eV from the white line energy. XANES provides information on the local site
 905 symmetry of the absorbing atom, bond distance distribution and sort of neighbouring atoms on the
 906 medium range scale. The extended X-ray absorption fine structure (EXAFS) corresponds to the
 907 energy region that extends ~1000 eV from the absorption edge. EXAFS is highly sensitive to the
 908 distribution and sort of nearest-neighboring atoms.

909 XANES and EXAFS spectra of Kr retained in quenched Fpc and $\text{Fe}_{88}\text{S}_{12}$ (blue spectra,
 910 Cell_1 and Cell_7 Table 1) are presented in Figure S3 and S4. Comparison of these two spectra
 911 reveals a well-structured first XANES peak region in both spectra, as well as an energy shift of the
 912 white line. Despite the absence of a simple theoretical interpretation of the XANES spectra,
 913 important information is commonly extracted through the comparison to reference spectra
 914 measured on known materials as well as from full multiple scattering calculations.

915 In a first step, we compared the XANES spectra acquired in quenched samples to reference
 916 spectra of pure Kr in the gaseous, liquid and solid state collected at different pressures (black
 917 spectra, Figure S4). We observed a clear similarity between the spectra of Kr retained in quenched
 918 samples with those of liquid and solid krypton. This suggests that Kr could partly be coordinated
 919 to another Kr in a similar symmetrical arrangement as pure liquid or solid fcc Kr under pressure.

Supplementary Information

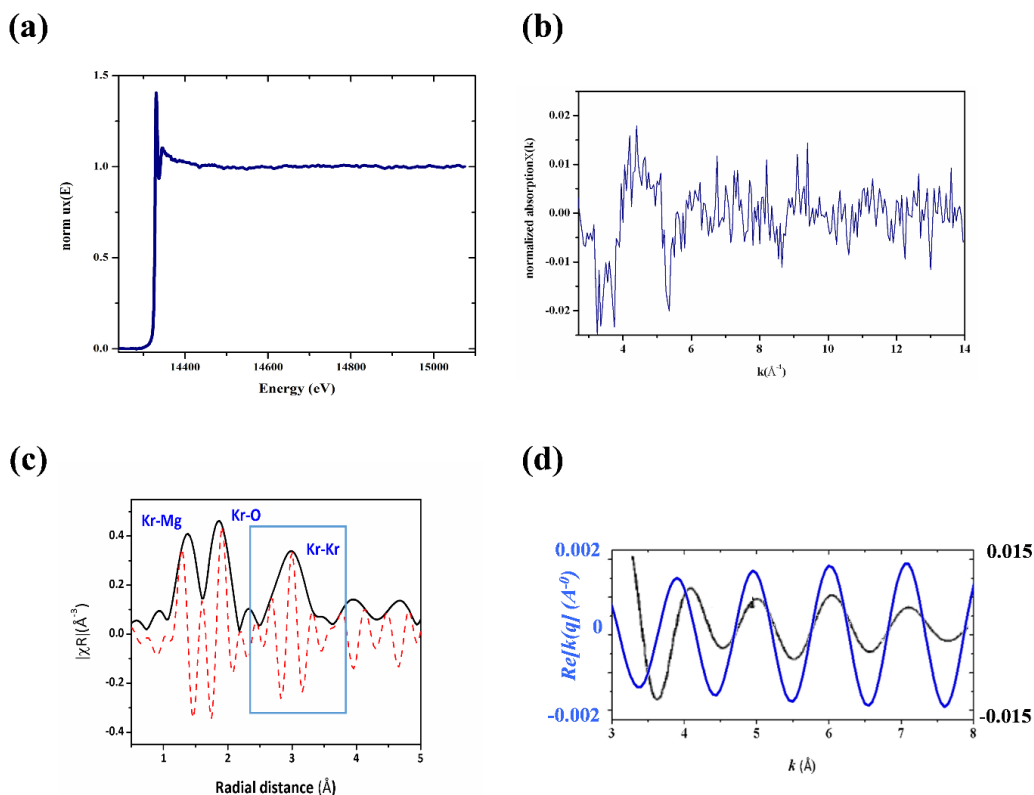
To better interpret the experimental XANES data and constrain the structural incorporation mechanism of Kr, we conducted full multiple scattering calculations (FMS) using the Feff9 code (Rehr et al., 2010). FMS XANES spectra were computed at the Kr K-edge for a single Kr atom replacing the anion or cation in MgO and FeO. Calculations were performed on a sphere having a FMS radius of 6 Å. For the self-consistent loop, a cluster of 3.1 Å and a convergence after 30 iterations were chosen. The core hole was calculated after the final state rule and the scattering amplitude was fixed to unity for all calculations. The XANES spectra were calculated with a fine grid of 0.05 eV. The exchange-correlation potential for the fine structure and the atomic background were computed using the Hedin-Lundquist formalism and the ground state.

The resulting calculated XANES spectra for Kr incorporated in MgO in FeO and in (Mg,Fe)O are shown in Figure S5. It is worth noting that only those spectra calculated for Kr replacing the oxygen site in FeO show similarities to the experimental spectra. They indeed exhibit a comparable white line slope and first XANES peak shape (Figure S5). These similarities in the XANES data imply that Kr atoms in the quenched samples may be entrapped in oxygen vacancies of Fpc having Mg and Fe as next-nearest neighbor. Such Kr substitution for neutral Schottky oxygen vacancies has been previously suggested by Martin et al. (2015) from X-ray absorption data on ion-implanted UO₂. In contrast, the calculated spectra of Kr replacing Mg and Fe do not match with the measured Kr K-edge XANES data. This discards this type of substitution mechanism in the quenched samples.

To estimate the Kr next nearest neighbor bond distances in the quenched samples, we used the energy shift of the first XANES peak in the acquired spectra following the approach of DiCicco et al. (1996). Calculated pressures are in the range of 0.5-5 GPa (Figure S6). This matches the experimental XANES measurements and suggests that the Kr impurity atoms are enclosed under a positive confinement pressure or stress. Similar pressures have been reported for Kr ion-implanted metal foils MgO and UO₂ (Tan et al., 1991; Norton et al., 1992; Martin et al., 2015;).

Based on these observations, we propose that Kr impurity clusters may have formed during *P/T* quenching. The significant expansion of Kr (more than 50% during P quenching from 40-60 GPa (Rosa et al., 2018) may favor short range diffusion of initially homogeneously distributed Kr atoms and their precipitation into NG nano-impurity clusters. This short range diffusion and lattice rearrangement may be driven by the lattice strains that Kr atoms exert on the host lattice at room conditions. It has been previously shown that structures hosting large impurity atoms tend to form impurity clusters by a point defect coalescence mechanism. This mechanism allows reducing the tensile stresses by transforming them in compressive ones that are energetically more favorable for the structure (Noordhuis and De Hosson, 1991). The general observation of low diffusivities of NGs at ambient pressure and high temperature in crystals (*i.e.*, Kr: $1.92 \times 10^{-22} \text{ m}^2 \text{ s}^{-1}$ in UO₂ at 1273 K; Michel, 2011) further supports a dissolution mechanism based on short range diffusion and lattice rearrangement. Such mechanism also operates for trace elements that tend to concentrate in defect structures in strained crystal (Piazolo et al., 2016).

Supplementary Information



958

959 **Figure S3.** (a) Extended normalized K-edge X-ray absorption spectrum of Kr entrapped in
 960 quenched Fpc (~3 wt.% of Kr, Cell_1), (b) its extracted EXAFS function $\chi(k)$ and (c) its Fourier
 961 transformation showing the mean distances of neighbouring atoms to the central absorbing Kr
 962 atom in Å (phase shifted). Potential neighbouring atoms and bond configurations are assigned
 963 above the three main peaks that are only based on ionic radii considerations. (d) shows the real
 964 part of the Fourier back transformation (dark blue curve) obtained from the FT region between
 965 2.5 and 3.5 Å that is indicated as blue box in (c). The back FT is compared to the theoretical Kr-
 966 Kr single scattering path reported for solid Krypton at 8 GPa by [DiCicco et al. \(1996\)](#) (black
 967 curve). It is worth noting the agreement between minima and maxima positions at high k and the
 968 pronounced differences in amplitude between the back FT function of this study and the theoretical
 969 Kr-Kr single scattering path: For Kr entrapped in Fpc the amplitude of the EXAFS function is
 970 significantly smaller (± 0.002) than the one of pure fcc Kr (± 0.015). This difference in amplitude
 971 indicates high structural disorder around Kr entrapped in Fpc.

Supplementary Information

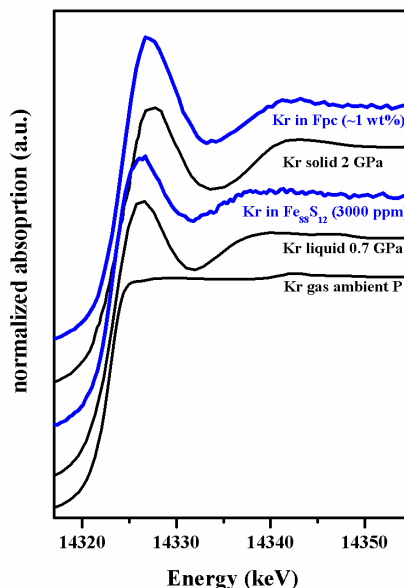


Figure S4. Selected K-edge XANES spectra of Kr entrapped in Fpc and Fe-S alloy (cell_1, cell_7, blue spectra) compared to spectra of monoatomic Kr in the gas, liquid and solid state at different pressures (black spectra) from DiCicco et al. (1996). Kr is in the gas state at ambient pressure, liquid up to 0.85 GPa and solidifies beyond this pressure into a fcc structure. The gaseous Kr XANES spectrum is featureless after the absorption edge. The little elevation at 14340 eV is due to a double excitation process. The liquid Kr XANES spectrum is characterized by a strong white line peak and a second smaller XANES peak. Compared to liquid Kr, the white line position and the position of the second XANES peak of the solid pure fcc Kr spectrum are shifted to higher energies. The spectra obtained of Kr retained in quenched samples is situated between the liquid and solid fcc Kr in terms of white line energy position and position of the second XANES peak. The slope between the first minima after the first XANES peak and the second XANES peak is steeper in pure Kr than in entrapped Kr.

Supplementary Information

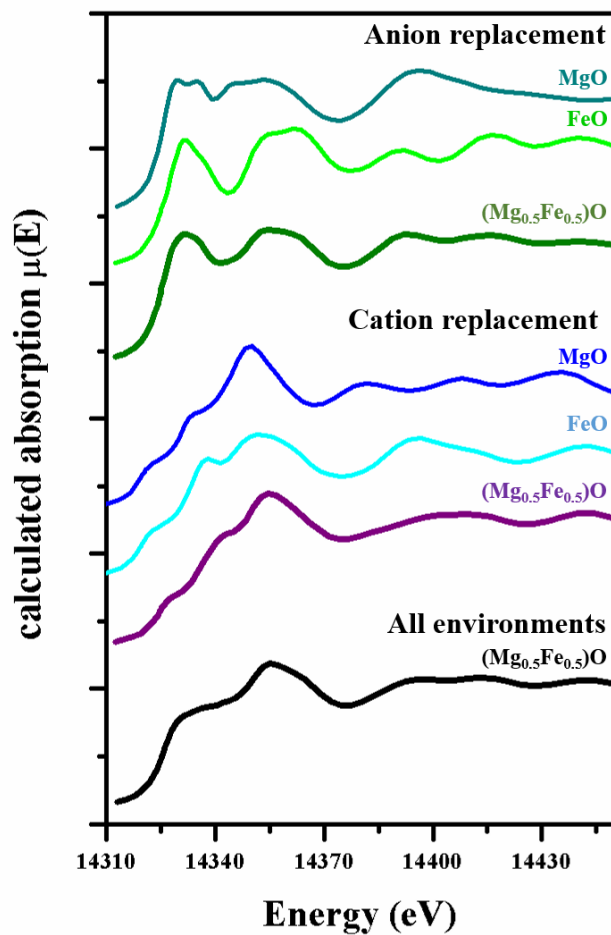


Figure S5. Calculated Kr K-edge XANES spectra for a single Kr atom incorporated in MgO, FeO and $\text{Mg}_{0.5}\text{Fe}_{0.5}\text{O}$. Green and blue spectra show the calculation results for Kr substituting in the anion site (O^{2-}) and in the cation site (Mg^{2+} and Fe^{2+}), respectively. The black spectrum is the sum over all calculated Kr environments in $\text{Mg}_{0.5}\text{Fe}_{0.5}\text{O}$.

Supplementary Information

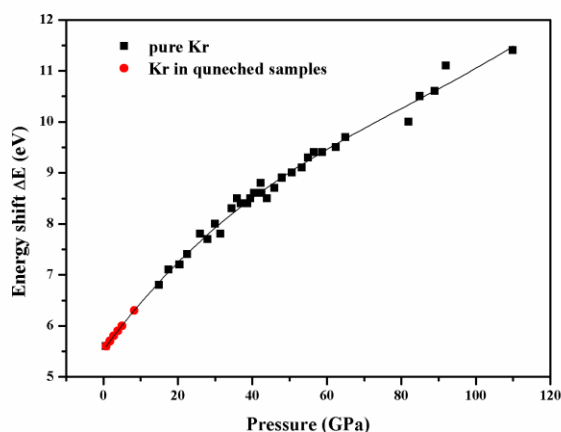


Figure S6. Energy shift of the first XANES peak (ΔE in eV) of monoatomic fcc Kr (black squares) and Kr entrapped in quenched phases (red circles) as a function of pressure. Data for pure fcc Kr are taken from [Rosa et al. \(2018\)](#). The energy shift can directly be related to the interatomic distance between two Kr atoms as described by [DiCicco et al. \(1996\)](#). The black line shows a third order polynomial function fitted to the data of [Rosa et al. \(2018\)](#), with $\Delta E = 5.525 + 0.09967 \cdot P + 7.52e-4 \cdot P^2 + 3.08e-6 \cdot P^3$, where P is the pressure in GPa. The individual pressures in the Kr clusters entrapped in quenched samples could be deduced using this fit function and the energy shift obtained from the experimental spectra of Kr retained in the quenched phases (red circles).

6. Lattice strain model approach and parameters

We conducted lattice strain modelling following the established method of [Blundy and Wood \(2003\)](#) to estimate solubilities of Ne, Ar, Kr and Xe throughout the lower mantle from 25 to 120 GPa and 1800 to 2500 K:

$$c_i = c_0 \times \exp \left\{ \frac{-4\pi N_A E_m \left[\frac{1}{2} r_0 (r_i - r_0)^2 + \frac{1}{3} (r_i - r_0)^3 \right]}{RT} \right\}$$

Here, c_i is the solubility of element i with radius r_i , c_0 is the maximal solubility of the host site, N_A is the Avogadro's number, E_m is the Young's modulus which provides the flexibility of the site and r_0 is the host site radius. The elasticity of the host site, E_m is expressed by the relation: $E_m = (9 \cdot K_0 \cdot G_0) / (3 \cdot K_0 + G_0)$.

In previous studies that developed lattice strain models for noble gases, the high P/T experimental solubility data have been adjusted using ambient conditions NG radii (r_i) ([Brooker, 2003](#); [Shcheka and Keppler, 2012](#)). This approach results in unrealistically low values of the Young's moduli E_m , that are much smaller than the values calculated from the bulk elastic moduli at the conditions of the experiment.

For example, [Shcheka and Keppler \(2012\)](#) obtained a fitted E_m value of 35 GPa for the oxygen site in Bg, at 25 GPa and 1800 K. This value is close to the calculated Young's modulus of Bg at ambient condition ($E_m = 25$ GPa), but differs significantly from its calculated value at the experimental conditions of the uppermost lower mantle ($E_m = 440$ GPa). The host site at uppermost lower mantle conditions is significantly stiffer than at ambient conditions. This should be taken into account to fit and extrapolate solubility data to high P/T conditions.

We intended to establish lattice strain models to predict solubilities through the mantle for the suite of NGs. Therefore, we reduced the fitting parameters in the lattice strain models to c_0 and constrained E_m and $r_{0,i}$ to calculated values using thermoelastic and crystal-chemistry (coordination dependent atomic radii) data.

The oxygen host site radii in Fpc and Bg at ambient conditions were derived from [Shannon \(1976\)](#) by taking into account the coordination of the sites ([Zhang and Zhu, 1995](#)). In Fpc, oxygen is six-fold coordinated to cations and has an effective ionic radius of 1.4 Å. In Bg, oxygen is four-fold coordinated to cations but in two distinct crystallographic sites with different bond lengths, leading to an average site radius of 1.37(1) Å. Vacancy site radii ($r_{0,P,T}$) at high P/T conditions were obtained by calculating the high P/T structures from the thermal equation of states reported by [Mao et al. \(2011\)](#) for Fpc and by [Fiquet et al. \(2000\)](#) for Bg (**Table S2**). We noted that the solubility trends of Ar, Kr and Xe reported by [Shcheka and Keppler \(2012\)](#) at 25 GPa and 1800 K could not be reproduced with the ionic radius of oxygen in Bg and only with a crystal radius that is about 0.13 Å smaller. We therefore employed the crystal radii obtained at high P/T conditions for Bg.

Neutral atomic effective radii of NGs at ambient conditions from Ne to Xe were evaluated using the ionic radii reported by [Zhang and Zhu \(1995\)](#). For Ar, Kr and Xe, we extrapolated the ionic radii for the [4]-fold coordination using the available data for the [6]- and [8]-fold

Supplementary Information

coordination. The relative volume reduction of zero-charged radii at high P/T conditions were obtained from those of pure NGs using the thermal equation of states listed in Table S3. The resulting radii are also listed in Table S3.

We employed values of E_m that have been calculated based on bulk elastic data corresponding to the high P/T conditions of the experiment using K_0 , G_0 and their P/T derivatives reported by Wang et al. (2004) (see Table S2). However, this approach does not account for the small difference in stiffness between a filled host site and a vacant site (Karato, 2016), which in general should be slightly more flexible. This may only affect NGs that exhibit large differences between their ionic radii and the ones of the host sites (*i.e.*, Ne, Xe in the present case). This could in turn lead to a slight underestimation of their solubilities, which is however not relevant in the present case as maximal solubilities are always used. This effect may become an important factor for solubility data obtained at high dilution levels.

Our lattice strain model approach contains only one fitting parameter that is the maximal site solubility c_0 . For the oxygen site in Fpc c_0 was adjusted using the Kr solubility data obtained in the present study as anchoring points (Figure 5a). Solubilities of Ar, Kr and Xe obtained at 25 GPa and 1800 K were used to fit c_0 for Bg. Due to the absence of solubility data at higher P/T conditions for NGs in Bg, the value of c_0 obtained at 25 GPa and 1800 K was subsequently employed for the Bg lattice strain models at 50 and 120 GPa.

The combination of $E_{P,T}$, $r_{0,P,T}$ and $r_{i,P,T}$ in our lattice strain model reproduces well the experimentally observed solubility trend from light to heavy NGs reported by Shcheka and Keppler (2012) (Figure 7, bold black dotted line for Mg(Si,Al)O₃). The fitted c_0 value is in good agreement with the one obtained by Shcheka and Keppler (2012). Our approach takes into account the compressibility of NGs, the type of host site and change in stiffness of a site with P/T . This is important because these parameters change significantly at LM conditions. We therefore conclude that, for highly compressible NGs, the present approach is appropriate and can be used for predicting NG solubilities in a host lattice site at the extreme P/T conditions of the lower mantle and beyond.

Table S2. Lattice strain model input parameters used to calculate NG solubilities at high P/T conditions in Fpc and Bg.

P GPa	T K	Fpc			r_i [6]					Bg			r_i [4]				
		c_0	$r_{0,P,T}$	E_m	He	Ne	Ar	Kr	Xe	c_0	$r_{0,P,T}$	E_m	He	Ne	Ar	Kr	Xe
0	298	1.53	1.4	18	1.08	1.21	1.64	1.78	1.96	0.9	1.37	25	0.9	1.18	1.51	1.69	1.89
25	1900	1.1	1.26	306	1.04	1.10	1.31	1.33	1.50	0.54	1.21	440	0.86	1.07	1.20	1.27	1.44
50	1900	1.9	1.19	440.2	1.04	1.09	1.22	1.25	1.40	0.54	1.19	552.5	0.86	1.06	1.12	1.19	1.35
120	2500	2.6	1.12	777.5	1.00	1.06	1.13	1.15	1.29	0.54	1.17	866.5	0.84	1.03	1.04	1.10	1.24

Table S3. Thermo-elastic parameters for Mie-Grüneisen equation of states after Jackson and Ridgen (1996) or Dewaele et al. (2008) used to calculate NG radii at high P/T conditions.

	V_0	K_0	K'	Θ_D	γ_0	γ_1
Ne ^a	88.98	1.4	8.03	75.1	0.97	2.44
Ar	149.8 ^b	2.b	7.59 ^b	93.3 ^c	0.5 ^{fixed}	2.2 ^c
Kr	220.61 ^d	1.65 ^d	6.7 ^d	79.1 ^c	0.5 ^{fixed}	2.17 ^c
Xe	270 ^e	2.18 ^e	6.26 ^e	57 ^c	0.5 ^{fixed}	2.36 ^c

^a all parameters taken from Dewaele et al. (2008); ^b from Dewaele et al. (2018); ^c from Jephcoat (1998); ^d from Rosa et al. (2018); ^e from Rosa et al. (in prep.).

Supplementary Information

7. Formation of volatile saturated liquid/melt phase during magma ocean crystallization

Presently, two models describing the crystallization of the magma ocean (MO) in the deep primitive Earth have been reported: (1) the classical solidification model from the bottom to the top (Solomatov and Stevenson, 1993) and (2) the more recent model that proposes the onset of solidification in the mid-mantle (Labrosse et al., 2007). For both models crystallization of LM minerals at NG saturated conditions may have occurred.

In the classical bottom-up crystallization model of Solomatov and Stevenson (1993), volatiles are incorporated in solidifying minerals in small quantities. The majority of volatiles are enriched and saturate in solution in residual liquids as solidification proceeds. Then, volatile-rich liquids rise to the surface where they form bubbles. If the size of the bubbles remains below 1 mm, they are re-entrained in the flow of the convecting MO and resorbed at depth (Elkins-Tanton, 2008).

In the second model, buoyant crystals of the first forming solid phase (Fe-poor Bg) accumulate on the top of the LM and Fe-rich residual melt. This leads to an early chemical decoupling of the LM from the upper mantle (UM). Upon further crystallization and cooling, the basal Fe-rich melt saturates in volatiles. The early decoupling of the LM and UM is supported by geochemical observations on fissogenic Xe isotopes (Allègre et al., 1983; Pepin and Porcelli, 2006; Mukhopadhyay, 2012).

8. NG replenishment model and considered isotopic Ne signatures therein

In our model, we assumed that only the lower mantle has captured a solar-wind irradiated Ne isotope signature (Neon-B) after the moon-forming impact, with a $^{20}\text{Ne}/^{22}\text{Ne}$ ratio of 12.73 (Eberhart et al. 1972). We also presumed that the atmosphere has entirely lost its Neon-B signature during the moon-forming impact and that the residual atmosphere (residual Ne comprises 0.7% of primordial atmosphere) is Q-like with a $^{20}\text{Ne}/^{22}\text{Ne}$ ratio of ~ 10.5 . In our model, the present-day atmospheric $^{20}\text{Ne}/^{22}\text{Ne}$ ratio of ~ 9.8 is considered as a mix of Neon-B (30.4%), residual Q-like signature (0.7%) and planetary component with a $^{20}\text{Ne}/^{22}\text{Ne}$ ratio of 8.5 (68.9%) that was delivered during late-veneer by comets and meteorite (Marty, 2012). In our model, we supposed that the Ne signature of comets is Q-like, as it is for meteorites. This was proposed by Marty et al. (2008) based on measurements of refractory grains in comets. Measured Ne abundances in the comet 67P, revealed concentrations below the detection limit, showing that Ne was not trapped in cometary ice. In the present scenario, the solar Ne component found for MORBs and CO₂ wells (Eberhart et al. 1972) may then be explained by subduction of atmospheric Ne after lower mantle outgassing.

Supplementary Information

9. References

- Allègre, C.J., Staudacher, T., Sarda, P., Kurz, M., 1983. Constraints on evolution of Earth's mantle from rare gas systematics. *Nature* 303, 762–766, DOI: <https://doi.org/10.1038/303762a0>.
- Akawama, Y., Kawamura, H., 2004. High-pressure Raman spectroscopy of diamond anvils to 250 GPa: Method for pressure determination in the multimegabar pressure range. *Journal of Appl. Phys.*, 96, 3748, DOI: <https://doi.org/10.1063/1.1778482>.
- Ashcroft, N.W., Lekner, J., 1966. Structure and Resistivity of Liquid Metals. *Phys. Rev.* 145, 83, DOI: <https://doi.org/10.1103/PhysRev.145.83>
- Blundy, J., Wood, B., 2003. Partitioning of trace elements between crystals and melts. *Earth Planet. Sci. Lett.*, 210, 383-397, DOI: [https://doi.org/10.1016/S0012-821X\(03\)00129-8](https://doi.org/10.1016/S0012-821X(03)00129-8).
- Brooker, R.A., Du, Z., Blundy, D.J., Kelley, S.P., Allan, N.L., Wood, B.J., Chamorro, E.M., Wartho, J.A., Purton, J.A., 2003. The ‘zero charge’ partitioning behaviour of noble gases during mantle melting. *Nature*, 423, 738–741, DOI: <https://doi.org/10.1038/nature01708>.
- Dewaele, A., Datchi, F., Loubeyre, P., Mezouar, M., 2008. High pressure-high temperature equations of states of neon and diamond. *Phys. Rev. B.*, 77, 094106, DOI: <https://doi.org/10.1103/PhysRevB.77.094106>.
- Dewaele, A., Torrent, M., Loubeyre P., Mezouar, M., 2008. Compression curves of transition metals in the Mbar range: Experiments and projector augmented-wave calculations. *Phys. Rev. B*, 78, 104102, DOI: <https://doi.org/10.1103/PhysRevB.78.104102>.
- Dewaele, A.D., Loubeyre, P., Occelli, F., Marie, O., Mezouar, M., 2018. Toroidal diamond anvil cell for detailed measurements under extreme static pressures. *Nature Com.*, 9, 2913, DOI: <https://doi.org/10.1038/s41467-018-05294-2>.
- DiCicco, A., Filippono, A., Itié, J.P., Polain, A., 1996. High-pressure EXAFS measurements of solid and liquid Kr. *Phys. Rev. B* 54, 13, 9086-9098, DOI: <https://doi.org/10.1103/physrevb.54.9086>
- Eberhart, P., Geiss, J., Graf, H., Groegler, N., Mendia, M.D., Moergeli, M., Schwaller, H., Stettler, A., Kraehenbuehl, U., Von Guten, H.R., 1972. Trapped solar wind noble gases in Apollo 12 lunar fines 12001 and Apollo 11 breccia 10046. *Physikalisches Institute Bern*, DOI: [https://doi.org/10.1016/0016-7037\(73\)90001-X](https://doi.org/10.1016/0016-7037(73)90001-X).
- Elkins-Tanton, L.T., 2008. Linked magma ocean solidification and atmospheric growth for Earth and Mars. *Earth Planet Sci Lett.*, 271, 1–4, 181-191. DOI: <https://doi.org/10.1016/j.epsl.2008.03.062>.
- Fiquet, G., Dewaele, A., Andrault, D., Kunz, M., Le Bihan, T., 2000. Thermoelastic properties and crystal structure of MgSiO₃ perovskite at lower mantle pressure and temperature conditions. *Geophys. Res. Lett.*, 27(1), 21– 24, DOI: <https://doi.org/10.1029/1999GL008397>.
- Giampaoli, R., Kantor, I., Mezouar, M., Boccato, S., Rosa, A.D., Torchio, R., Garbarino, G., Mathon, O. Pascarelli, S., 2018. Measurement of temperature in the laser heated diamond anvil cell: comparison between reflective and refractive optics. *High Pres. Res.*, 250-269, DOI: <https://doi.org/10.1080/08957959.2018.1480017>.
- Huang, H., Wu, S., Hu, X., Wang, Q., Wang, X., Fei, Y., 2013. Shock compression of Fe-FeS mixture up to 204 GPa. *Geophys. Res. Letters* 40, 687-691, DOI: <https://doi.org/10.1002/grl.50180>

Supplementary Information

- 1147 Jackson, I, Rigden, S. M., 1996. Analysis of P-V-T data: constraints on the thermoelastic properties
1148 of high pressure minerals. *Physics of Earth and Planet. Int.*, 96, 85-112, DOI:
1149 DOI:10.1016/0031-9201(96)03143-3.
- 1150 Jephcoat, A.P., 1998. Rare-gas solids in the Earth's deep interior. *Nature* 393, 355-358, DOI:
1151 <https://doi.org/10.1038/30712>.
- 1152 Karato, S-I., 2016. Physical basis of trace element partitioning: A review. *Am. Mineral.*, 101,
1153 2577-2593, DOI: <https://doi.org/10.2138/am-2016-5665>.
- 1154 Kantor, I., Marini, C., Mathon, O., Pascarelli, S., 2018. A laser heating facility for energy-
1155 dispersive X-ray absorption spectroscopy. *Rev. Sci. Instrum.*, 89, 013111, DOI:
1156 <https://doi.org/10.1063/1.5010345>.
- 1157 Labrosse, J.W., Hernlund, N., Coltice, A., 2007. A crystallizing dense magma ocean at the base of
1158 the Earth's mantle. *Nature*, 450, 866–869, DOI: <https://doi.org/10.1038/nature06355>.
- 1159 Mao, Z., Lin, J.-F., Liu, J., Prakapenka, V.B., 2011. Thermal equation of state of lower-mantle
1160 ferroperrite across the spin crossover. *Geophys. Res. Lett.*, 38, L23308, 1-4, DOI:
1161 <https://doi.org/10.1029/2011GL049915>.
- 1162 Mathon, O., Beteva, A., Borrel, J., Bugnazet, D., Gatla, S., Hino, R., Kantor, I., Mairs, T., Munoz,
1163 M., Pasternak, S., Perrin, F., Pascarelli S., 2015. The time-resolved and extreme conditions
1164 XAS (TEXAS) facility at the European Synchrotron Radiation Facility: the general-purpose
1165 EXAFS bending-magnet beamline BM23. *J. Synchrotron Radiat.*, 22(1), 1548–1554, DOI:
1166 <https://doi.org/10.1107/S1600577515017786>.
- 1167 Martin, P.M., Vathonne, E., Carlot, G., Delorme, R., Sabathier, C., Freyss, M., Garcia, P., Bertolus,
1168 M., Glatzel, P., Proux, O., 2015. Behavior of fission gases in nuclear fuel: XAS
1169 characterization of Kr in UO₂. *J. Nucl. Mater.*, 466, 379-392, DOI:
1170 <https://doi.org/10.1016/j.jnucmat.2015.08.019>.
- 1171 Marty, B., 2012. The origins and concentrations of water, carbon, nitrogen and noble gases on
1172 Earth. *Earth Planet. Sci. Lett.*, 313-314, 56-66, DOI:
1173 <https://doi.org/10.1016/j.epsl.2011.10.040>.
- 1174 Marty, B., Palma, R.L., Pepin, R.O., Zimmermann, L., Schlutter, D.J., Burnard, P., Westphal, A.J.,
1175 2008. Helium and Neon abundances and compositions in cometary matter. *Science*, 319, 75-
1176 78, DOI: <https://doi.org/10.1126/science.1148001>.
- 1177 Michel, A., 2011. Etude Du Comportement Des Gaz de Fission Dans Le Dioxyde D'uranium :
1178 Mécanismes de Diffusion. Nucleation et Grossissement de Bulles (Phd thesis), University of
1179 Caen, France.
- 1180 Mukhopadhyay, S., 2012. Early differentiation and volatile accretion recorded in deep mantle neon
1181 and xenon. *Nature*, 486, 101-104, DOI: <https://doi.org/10.1038/nature11141>.
- 1182 Noordhuis, J., De Hosson, J. Th.M., 1991. Fundamental and applied aspects of noble gas bubbles
1183 in steel. Edited by S.E. Donnelly and J.H. Evans. Plenum Press. New York, p. 153-165, DOI:
1184 https://doi.org/10.1007/978-1-4899-3680-6_13.
- 1185 Norton, M.G, Carter, C.B., Fleischer, E., Mayer, J.W., 1992. Solid krypton in MgO. *J. Mat. Res.*,
1186 7, 12, DOI: <https://doi.org/10.1557/JMR.1992.3171>.
- 1187 Pascarelli, S., Mathon, O., Mairs, T., Kantor, I., Agostini, G., Strohm, C., Pasternak, S., Perrin, F.,
1188 Chapellet, P., Clavel, C. (2016) The Time-resolved and Extreme-conditions XAS (TEXAS)
1189 facility at the European Synchrotron Radiation Facility: the energy-dispersive X-ray
1190 absorption spectroscopy beamline ID24. *Journal of Synchrotron Radiation* 23(1), 353-68,
1191 DOI: DOI: <https://doi.org/10.1107/S160057751501783X>.

Supplementary Information

- Pepin, R. O., Porcelli, D., 2006. Xenon isotope systematics, giant impacts, and mantle degassing on the early Earth. *Earth Planet. Sci. Lett.*, 250 (3-4), 470-485, DOI: <https://doi.org/10.1016/j.epsl.2006.08.014>.
- Piazolo, S., La Fontain, A., Trimby, P., Harley, S., Yang, L., Armstrong, R., Cairney, J.M., 2016. Deformation-induced trace element redistribution in zircon revealed using atom probe tomography. *Nature Com.*, 7, 10490, 1-7, DOI: <https://doi.org/10.1038/ncomms10490>.
- Polian, A., Itié, J.P., Dartyge, E., Fontaine, A., Tourillon G., 1989. X-ray absorption spectroscopy on solid krypton up to 20 GPa. *Physical Review B* 39, 5, 3369-3373, DOI: <https://doi.org/10.1103/physrevb.39.3369>
- Posner, E. S., Rubie, D.C., Frost, D. J., Vlcek, V., Steinle-Neumann, G., 2017. High P–T experiments and first principles calculations of the diffusion of Si and Cr in liquid iron. *Geochimica Cosmochimica Acta*, 203, 323-342, DOI: <https://doi.org/10.1016/j.gca.2017.01.024>.
- Rehr, J.J., Kas, J.J., Vila, F.D., Prange, M.P., Jorissen, K., 2010. Parameter-free calculations of X-ray spectra with FEFF9. *Physical Chemistry Chemical Physics* 7, 12, 5503. DOI: <https://doi.org/10.1039/B926434E>
- Rosa, A.D., Garbarino, G., Briggs, R., Svitlyk, V., Morard, G., Bouhifd, M.A., Jacobs, J., Irifune, T., Mathon, O., Pascarelli, S., 2018. Effect of the fcc-hcp martensitic transition on the equation of state of solid krypton up to 140 GPa. *Physical Rev. B* 97, 094115, DOI: <https://doi.org/10.1103/PhysRevB.97.094115>.
- Rosa, A.D. et al., (in prep). Martensitic transition and equation of state of Xe to 160 GPa.
- Shannon, R. D., 1976. Revised Effective Ionic Radii and Systematic Studies of Interatomic Distances in Halides and Chalcogenides. *Acta Crystallographica*, A32, 751-767, DOI: <https://doi.org/10.1107/S0567739476001551>.
- Shcheka, S.S., Keppler, H., 2012. The origin of the terrestrial noble-gas signature. *Nature*, 490, 531–534, DOI: <https://doi.org/10.1038/nature11506>.
- Shen, G., Prakapenka, V.B., Rivers, M.L., Sutton, S.R., 2004. Structure of Liquide Iron at Pressures up to 58 GPa. *Phys. Rev. B*, 92, 18, 185701, 1-4, DOI: <https://doi.org/10.1103/PhysRevLett.92.185701>
- Solomatov, V.S., Stevenson, D.J., 1993. Nonfractional crystallization of a terrestrial magma ocean. *J. Geophys. Res.* 98, 5391–5406, DOI: <https://doi.org/10.1029/92JE02579>.
- Tan, Z. Budnick, J.I., Pease, D.M., Namavar, F., 1991. X-ray absorption of krypton precipitates in solid matrices. *Phys. Rev. B* 43, 3, 1987-1992, DOI: <https://doi.org/10.1103/physrevb.43.1987>.
- Wang, Y., Weidner, D.J., Liebermann, R.C., Zhao, Y., 2014. P – V – T equation of state of (Mg,Fe)SiO₃ perovskite: constraints on composition of the lower mantle. *Physics Earth Planet Int.*, 83, 13-40, DOI: [https://doi.org/10.1016/0031-9201\(94\)90109-0](https://doi.org/10.1016/0031-9201(94)90109-0).
- Zhang, Y., Zhu, X., 1995. Atomic radii of noble gas elements in condensed phases. *Am. Min.* 80, 670-675, DOI: <https://doi.org/10.2138/am-1995-7-807>.